

AUTOMATIC PARTICLE TRACKING  
IN A THREE-DIMENSIONAL FLOW FIELD

by

ROBERTO GIACOMO RACCA  
B.Sc., University of Victoria, 1982

A THESIS SUBMITTED IN PARTIAL FULFILLMENT  
OF THE REQUIREMENTS FOR THE DEGREE OF

MASTER OF SCIENCE

in the Department


of

Physics


ACCEPTED  
FACULTY OF GRADUATE STUDIES

DATE Oct 31, 85 DEAN

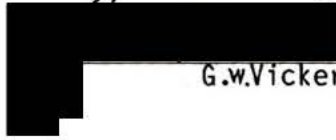
We accept this thesis as conforming  
to the required standard

  
J.M. Dewey

  
R.M. Clements

  
D.K. Walker

  
D.E. Hewitt

  
G.w.Vickers

© ROBERTO GIACOMO RACCA, 1985

UNIVERSITY OF VICTORIA

June 1985

*All rights reserved. This thesis may not be reproduced  
in whole or in part, by mimeograph or other means,  
without the permission of the author.*


Supervisor: Dr. John M. Dewey


### ABSTRACT


A technique has been developed whereby the three-dimensional motion of tracers in a fluid flow is automatically analyzed. Simultaneous orthogonal views of the tracer-seeded flow were recorded by a single high speed cine camera through a split field mirror system, and successively converted to machine readable form by a video digitizer. The images were digitally enhanced to separate the tracers from the contrasting background even in conditions of poor picture quality. Algorithms were developed to match the projections of individual tracers in the two views, obtain the three-dimensional co-ordinates, follow the tracers from frame to frame and compute the velocity vectors along the particle trajectories. Eulerian information was derived from the pooled velocity data points by interpolation on a regular spatial grid.


Tests of the method on various types of particle trajectories obtained in a small water tunnel have shown that the tracking is reliable even for rapidly changing and closely spaced paths.

Examiners:

  
J.M. Dewey

  
R.M. Clements

  
D.K. Walker

  
D.E. Hewgill

  
G.W. Vickers

## TABLE OF CONTENTS

|  | <u>Page</u> |
|--|-------------|
| ABSTRACT.....  | ii          |
| TABLE OF CONTENTS.....                               | iii         |
| LIST OF TABLES.....                                  | v           |
| LIST OF FIGURES.....                                 | vi          |
| ACKNOWLEDGEMENTS.....                                | viii        |
| DEDICATION.....                                      | ix          |
| CHAPTER 1 INTRODUCTION.....                          | 1           |
| CHAPTER 2 ACQUISITION OF VISUAL DATA.....            | 9           |
| 2.1 Orthogonal-view optical system.....              | 9           |
| 2.2 Alignment of optics.....                         | 14          |
| 2.3 Image digitization.....                          | 18          |
| CHAPTER 3 IMAGE ANALYSIS.....                        | 23          |
| 3.1 Introduction.....                                | 23          |
| 3.2 Image enhancement by histogram modification..... | 25          |
| 3.3 Image segmentation.....                          | 30          |
| 3.4 Location of tracer images.....                   | 36          |
| 3.5 Image processing equipment and procedure.....    | 40          |
| CHAPTER 4 TRACER MOTION ANALYSIS.....                | 46          |
| 4.1 Matching of pairs.....                           | 46          |
| 4.2 Trajectory tracing.....                          | 56          |
| 4.3 Processing of the positional data.....           | 66          |

|   | <u>Page</u> |
|---|-------------|
| CHAPTER 5 TESTING AND EVALUATION.....                           | 78          |
| 5.1 Test flow channel.....                                      | 78          |
| 5.2 Testing runs.....   | 80          |
| 5.3 Evaluation of the method.....                               | 99          |
| BIBLIOGRAPHY.....   | 102         |
| APPENDIX A Derivation of the 'rubber sheet' transformation..... | 104         |
| APPENDIX B Derivation of the parallax correction equations..... | 111         |

LIST OF TABLES

Page

Table 1. Summary of Analysis Steps

7

## LIST OF FIGURES

|  | <u>Page</u> |
|--|-------------|
| Figure 1. Mirror arrangements for simultaneous viewing from orthogonal directions.   | 10          |
| Figure 2. Orthogonal-viewing mirror system.  | 12          |
| Figure 3. Lighting arrangements within the mirror system.  | 13          |
| Figure 4. Example of intensity histogram of a digitized image.   | 27          |
| Figure 5. Examples of intensity histograms of digitized images.  | 32          |
| Figure 6. Demonstration of the effect of point drop-out on the contouring of a cluster of bright pixels.                   | 39          |
| Figure 7. Typical image analysis sequence.   | 41          |
| Figure 8. Example of interactive editing of image data.  | 44          |
| Figure 9. Diagram of orthogonal-view optical system, showing location of optical axes relative to assigned cartesian axes. | 49          |
| Figure 10. Example of matching ambiguity for points coplanar with both virtual viewpoints.                                 | 51          |
| Figure 11. Graphical representation of a hypothetical three-step trajectory tracing process.                               | 59          |
| Figure 12. Sample orthographic output of the tracking program, with mathematically generated data.                         | 63          |
| Figure 13. Sample stereoscopic output of the tracking program.   | 64          |
| Figure 14. Scalar velocity maps from the helical trajectories of figure 12.  | 72          |
| Figure 15. Full-screen display of a velocity map from figure 14.   | 73          |
| Figure 16. Orthographic output of vectorial velocity field from the helical trajectories of figure 12.                     | 74          |
| Figure 17. Stereoscopic output of vectorial velocity field from the helical trajectories of figure 12.                     | 75          |

|   | <u>Page</u> |
|---|-------------|
| Figure 18. Test flow channel.   | 79          |
| Figure 19. Orthographic output of tracer paths in the unrestricted column.  | 83          |
| Figure 20. Stereoscopic output of the trajectories of figure 19.  | 84          |
| Figure 21. Stereoscopic output of vectorial velocity field for the flow in the unrestricted column.                         | 86          |
| Figure 22. Scalar velocity maps for the flow in the unrestricted column.  | 87          |
| Figure 23. Full-screen display of a typical velocity map for the unrestricted column flow.                                  | 88          |
| Figure 24. Orthographic output of tracer paths in the column restricted by a sharp-edged orifice.                           | 90          |
| Figure 25. Stereoscopic output of the trajectories of figure 24.  | 91          |
| Figure 26. Orthographic output of symmetrized tracer paths in the column restricted by a sharp-edged orifice.               | 92          |
| Figure 27. Stereoscopic output of the trajectories of figure 26.  | 93          |
| Figure 28. Stereoscopic output of vectorial velocity field for the symmetrized flow in the column restricted by an orifice. | 95          |
| Figure 29. Scalar velocity maps for the symmetrized flow in the column restricted by an orifice.                            | 96          |
| Figure 30. Full-screen display of a velocity map from figure 29 for a section near the bottom of the visible volume.        | 97          |
| Figure 31. Full-screen display of a velocity map from figure 29 for the section at the top of the visible volume.           | 98          |
| Figure 32. Geometrical layout for the 'rubber sheet' transformation equations.  | 105         |
| Figure 33. Geometrical layout for the parallax correction equations.  | 112         |

## ACKNOWLEDGEMENTS

I wish to acknowledge my gratitude to Dr. J.M. Dewey for his guidance and encouragement throughout this research project.

I would like to thank the staff of the Machine Shop for their skill and promptness in building the test channel, and Mr. Larry Scotten for lending me the mirror system.

To my family goes my deepest gratitude for having always given me their love, help and support.

## CHAPTER 1

### INTRODUCTION

Of the various methods of examining and measuring the characteristics of fluid flow, direct observation of the motion of tracers is undoubtedly the most easily implemented and versatile technique. For certain applications, the use of long exposure photography gives a useful record of both position and mean velocity of tracers. If the intensity of the light source during the recording time has a sharp rise and a progressive decay, as with an electrical discharge tube, then it is possible to interpret the direction of motion of the tracers from the brightness distribution along the tracer streaks. Special shutters that open quickly and then progressively reduce the aperture also achieve the same effect.

The use of high speed photography to obtain a time sequence of tracer locations is useful where precise knowledge of particle position at narrowly spaced time intervals is required. If a tracer can be identified in successive frames, then the velocity can be reconstructed with a time base equal to the framing period. A record of the position-time history of flow tracers gives not only the time resolved particle velocities throughout the flow field, but also, by application of the equations of conservation of energy and mass, the hydrostatic and dynamic pressures, and the density in a compressible flow (Dewey, 1971). However, the process of manually following particle trajectories from a series of photographs is tedious, and if several paths intersect it may

become difficult. The difficulty is compounded if the flow to be visualized is three-dimensional, because a single view of the tracer field is no longer sufficient.

When it is necessary to measure the position of tracers in space, two or more views of the test section, taken from different angles, must be correlated. The process of reconstructing the spatial position of a point from its location in each distinct view is the object of photogrammetry techniques. The most common photogrammetric methods use two views. Although the directions from which the views are taken can be set arbitrarily, the two preferred arrangements are stereoscopic and orthogonal images.

Stereoscopic image pairs are recorded using two adjacent lenses, whose separation is usually the same as the average spacing of the human eyes. Each lens produces its own image on film. Because the two views are taken from slightly different positions, there is a change in parallax between them. Relative positions of objects in the near field will exhibit a greater shift in the two views than objects in the far field. Information about the depth of the scene is therefore contained in the stereoscopic pair, in a form that the human mind is naturally trained to interpret. If each recorded view is presented to the corresponding eye, an observer will mentally reconstruct the original image in its full three-dimensionality. Unlike a holographic recording, however, the reconstructed image only shows the scene as seen from the particular vantage point at which the stereo camera was located.

Stereoscopic cinematography has been used by various investigators to visually describe turbulent patterns in boundary-layer flows (Praturi and Brodkey, 1978) and in mixing processes (Tatterson et al., 1980). In these studies the analysis consisted of direct observation at low framing rates of high-speed movies taken with a stereoscopic camera head. To obtain the three-dimensional effect from such movies a special projector head is used which superimposes on the screen the images for right and left view. Each view is 'coded' within the projection system either by colored filters (usually red for one view and blue for the other) or by polarizers oriented perpendicularly. The observer wears glasses with correspondingly colored filters or oriented polarizers, so that each image is only allowed to reach the appropriate eye.

Complex three-dimensional flow patterns can be visually analyzed with the above method, but only in qualitative form. To compute precisely the positions of the tracers, measurements taken separately in the two views must be correlated mathematically. Sheu et al. (1982) performed manual tracking and digitization of tracer positions in stereo pairs, followed by data reduction and plotting by computer. To simplify the task of associating pairs and following individual trajectories, they took advantage of the brain's natural capability of reconstructing stereo images by adding a stereoscope to the viewing and digitization system. The observer used the stereoscope to identify corresponding tracer images and acquire a feeling for their motion in space. He then digitized the co-ordinates of tracers in the stereo

movie in a fixed order to match the images in a stereoscopic pair and the corresponding tracers in successive frames. More recently, Chang and Tatterson (1983) presented a more sophisticated system in which the tasks of frame digitization, image correlation and trajectory tracing are entirely automatic. Their analysis system included image processing of cinematographic records to locate the tracer images, correlation of tracer positions in the two views and frame-to-frame tracking.

Stereoscopic photography has the practical advantages of using a simple optical accessory directly attached to the camera and of requiring access to only one side of the apparatus under study. In terms of accuracy of reconstruction, however, the method is relatively poor. Due to the short baseline between the two viewpoints, and consequently the small difference in parallax for objects in various planes, even small inaccuracies in locating the images in each view may lead to gross misplacement of points along the 'depth' dimension. This problem forced investigators (Sheu et al., 1982) to introduce empirical calibration curves in the reconstruction equations to reduce the error.

It would be possible to increase the accuracy of the stereoscopic method while still conserving most of its benefits by increasing the length of the baseline between the viewpoints. This would preclude the possibility of true-to-life scene reconstruction by observation through a stereoscopic projection system, since the parallax between views would be different from the one given by the normal spacing of human eyes. For photogrammetric analysis of the viewfield, on the other hand, the greater spacing would be perfectly acceptable since the reconstruction

algorithm has no preconceptions about the position of the 'eyes' that supply its data, provided their separation is known. By the same token, there is no requirement that the two axes of the optical system be parallel as they are in the usual stereoscopic arrangement.

The most advantageous geometry with non-parallel optical axes is the arrangement with perpendicular views. With this method, each view gives a virtually direct measurement of two of the three spatial coordinates of a tracer, one co-ordinate being common to both views. Unlike photogrammetry from stereoscopic images, orthogonal-view photogrammetry is not plagued by an intrinsically less accurate dimension which can only be measured indirectly from parallax relations. Orthogonal views have been used in various high speed photography applications where complex motion of objects must be analyzed. A recent example is Hyzer's (1984) study of the motion of a disc in a magnetic field, performed using a system of mirrors on an optical bench to record the two views on film as a split-image. The analysis of that experiment involved digitizing selected points of the disc's image in the two views and reconstructing their three-dimensional locations by computer.

An optical system that created overlapping perpendicular views was used by Caffyn and Underwood (1952) to measure velocity profiles in liquids by stroboscopic photography of tracers. The displacement between tracer images on film was analyzed with a travelling microscope. Winter (1958) adopted an orthogonal-view approach with separate camera positions to photograph the complex three-dimensional flow field in a

free jet. The method, however, is not as suitable as stereoscopy for direct visual analysis because the human mind is not well suited to correlating pairs of images taken from entirely different directions. The lack of obvious similarities between the two views makes the task of identifying and following individual tracers an arduous one without computer assistance. Because of this difficulty, the orthogonal-view analysis method has not enjoyed the same popularity as the stereoscopic method for three-dimensional flow visualization. Peskin (1972), as part of his doctoral thesis research, designed a perpendicular-view optical system which he used to obtain high speed cinematographic records of the motion of tracers in the in vitro flow through heart valves. Although he did not develop a full analysis method for data from such records, he did discuss some aspects of the reconstruction of spatial co-ordinates and the subsequent data processing.

In summary, orthogonal-view visualization of tracers in a three-dimensional flow field has the potential for maximum accuracy of measurement, but the manual digitization of a large number of tracers in non-stereoscopic pairs is difficult and tedious.

A system for the automatic analysis of orthogonal-view cinematographic records of tracer motion is the subject of this thesis. Table 1 gives a summary of the steps involved in the procedure. The method bears some affinity to the one used by Chang and Tatterson (1983), but has been developed specifically for perpendicular views. A report on some aspects of this system has been given by Racca and Dewey (1984). The visual data from experiments are recorded on film using a high

| TABLE 1<br><u>Summary of Analysis Steps</u>   |
|---|
| High speed photography of orthogonal views  |
| Video digitization of film  |
| Enhancement of images to locate tracers in each view  |
| Matching of tracer projections in the two views<br>to obtain three-dimensional co-ordinates |
| Tracking of spatial positions of tracers<br>in successive frames                            |
| Processing of the trajectory data   |

speed movie camera and an orthogonal-view optical system based on Peskin's (1972) design. The images on film are successively transferred to a computer as digitized matrices of intensity values. Three independent steps are then used to analyze these records. First, the digitized images are processed to isolate the tracers from the background and locate their centres in the two views. Both the brightness of the tracer images and the sharpness of their edges are used as recognition criteria, achieving a capability of interpreting even low-quality images. Next, the tracer positions in the two views are combined to yield three-dimensional locations. The matching process, which is based on similarity of location along the axis common to both views, includes compensation for parallax. The last step consists of following the displacement of individual tracers from frame to frame to map their trajectories. Further processing that computes tracer velocities along identified paths and interpolates the three-dimensional velocity field through the available data is also presented in this work.

The method has been tested on flow patterns generated in a small vertical water tunnel. Resin beads having density similar to that of water were used as tracers. Cine recordings were taken at framing rates of 100 to 200 pictures per second. Analysis examples will be shown for tracer motion in the steady flow through the unrestricted test section and in the unstable flow obtained downstream of a sharp-edged orifice.

## CHAPTER 2

### ACQUISITION OF VISUAL DATA

#### 2.1 Orthogonal-view optical system

In situations where the size of the observed volume allows it, the two perpendicular views required for reconstruction of the spatial positions of tracers are best recorded by a single camera through a suitable split-view system. This eliminates the problem of camera synchronization and reduces the overall cost of the equipment. For larger-scale applications, on the other hand, the use of separate cameras may be appropriate. Synchronization of separate image systems could be achieved easily by electronic means if video cameras were used, whereas conventional film cameras would require a linked feedback loop to control the speed of the drives.

Any optical system that can present two perpendicular views of the subject as adjacent images can be adopted in a single-camera arrangement. It is convenient to make the optical path length for the two views the same in order to have identical parallax in the two images and hence simplify the matching of features. Although prisms or optical fiber bundles might be used in specialized applications, mirrors appear preferable in most cases.

Mirror systems that perform the transformation from perpendicular to adjacent views have been used by various experimenters in different fields. Figure 1 shows two such arrangements, used by Hyzer (1984)

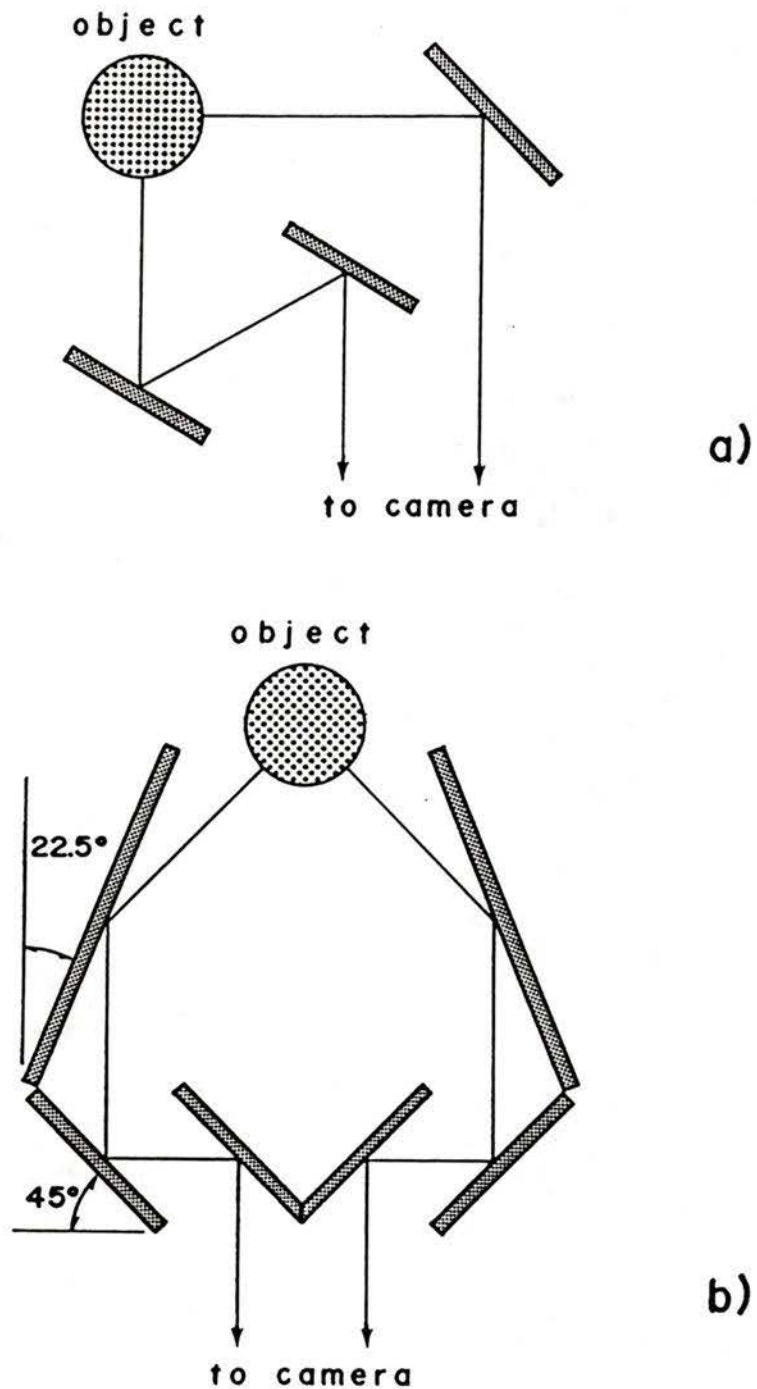


Figure 1. Mirror arrangements for simultaneous viewing from orthogonal directions, used by a) Hyzer (1984) and b) Peskin (1972).

(figure 1a) and by Peskin (1972) (figure 1b). In Hyzer's apparatus the mirrors are mounted on an optical bench, and their positions are adjusted to make the two optical path lengths equal for a given location of the object. Peskin's system lends itself to compact packaging in a self-contained device, suitable for observing a volume of several centimetres cross section. A suitable light source aimed at the object can be located in the central area of the arrangement without creating reflections that may reach the camera. Such a system was chosen for the work described in this thesis. Figure 2 shows the assembled optical device. All the mirrors were glass, front-surface aluminized, inserted into precise grooves in the wooden base that held them perpendicular to the same plane and in the proper geometrical layout. A metal lid, not shown in the photograph, protected the optical surfaces from dust. The lid and the base had a frontal cut-out that allowed insertion of the test section of a flow chamber in the appropriate position. The lid also had a central, square cut-out to accommodate a lighting device. A black frame facing the camera, with two adjacent openings for the two views, prevented stray light from reaching the lens. A threaded mount underneath the base was used to mount the device on a tripod. The useful field observable with this device was roughly 11 x 11 cm horizontally and 12 cm in height.

Several lighting devices were tried in the arrangement described above, with the goal of maximizing light intensity and uniformity while preventing reflections off the window surfaces from reaching the camera. Some of the possible geometries are shown in figure 3. In figure

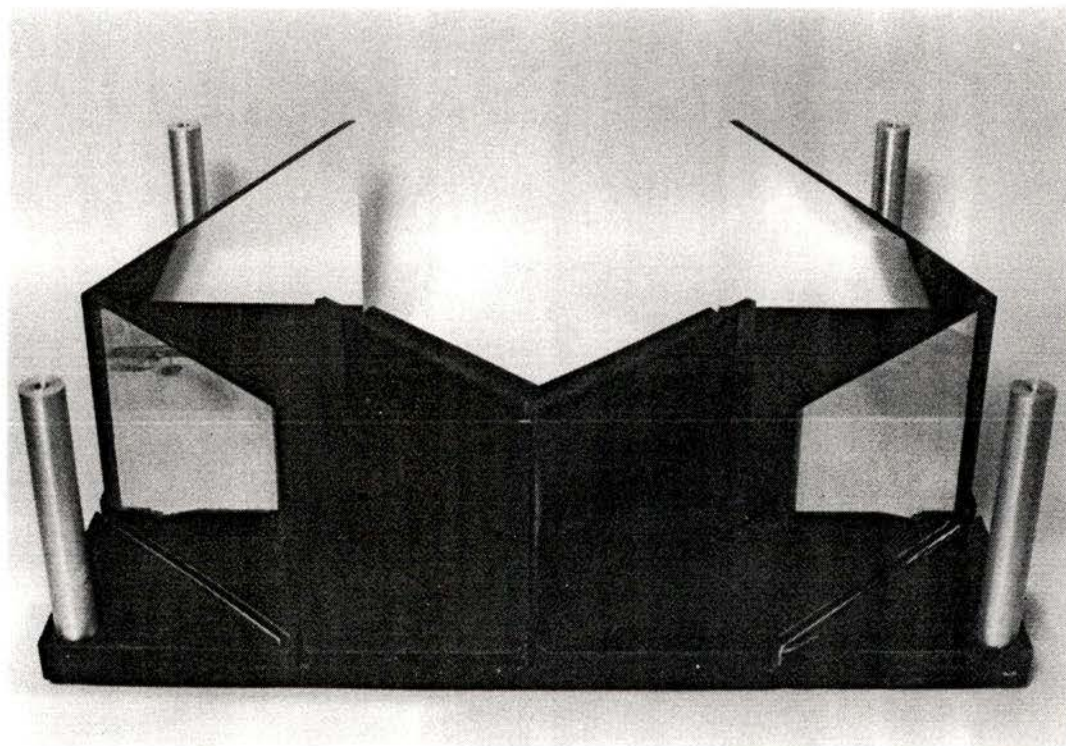
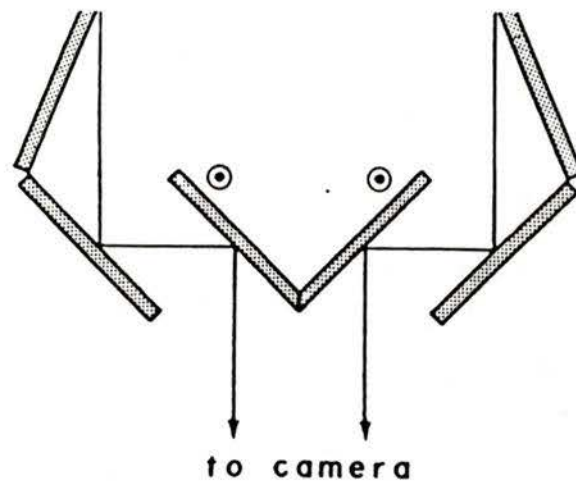
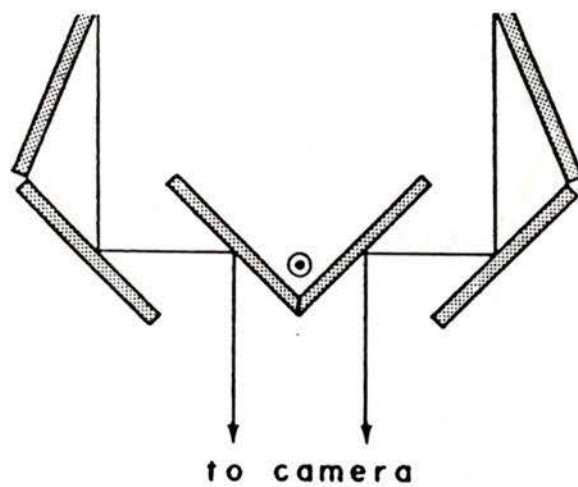


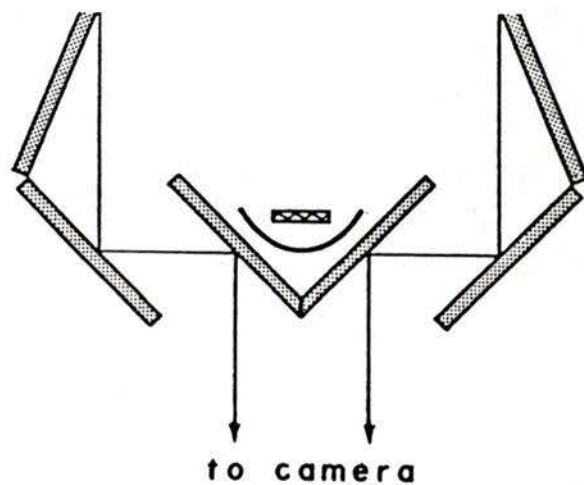
Figure 2. Orthogonal-viewing mirror system.



a)



b)



c)

Figure 3. Lighting arrangements within the mirror system:  
 a) two vertically-oriented linear quartz lamps;  
 b) one vertically-oriented linear quartz lamp;  
 c) one horizontal quartz lamp with reflector.

3a two 8-cm, 1000W linear vertically oriented quartz lamps, with no reflectors, were used. In figure 3b only one such lamp was used, located as far away as possible from the test chamber. With these lamps, forced air circulation by a small fan was necessary to prevent overheating, even for brief periods of operation. It was found that reflections from one area or other of the windows were unavoidable with these placements of the lamps, although they could be minimized by fine adjustment of their positions. Figure 3c shows a different approach which gave substantially better results. Here a single 800W Sylvania DXV quartz lamp housed horizontally in a 3-inch (diagonal) Bolex cine reflector was placed as far back as possible in the central area. The light intensity level obtained with this arrangement was lower than with either of the previous ones, but the uniformity was better and unwanted reflections could be almost entirely eliminated. The heat generated was tolerable without forced cooling for periods of operation up to 10 seconds with an off/on duty cycle of at least 2 to 1. The Bolex illuminator was eventually chosen as the most appropriate light source.

## 2.2 Alignment of optics

A number of fundamental rules had to be followed in setting up the optical system consisting of camera, mirrors and test section. Accurate reconstruction of the three-dimensional information from the recorded images depended on the observance of certain geometrical rela-

tions on which the photogrammetric analysis was based.

It is important to differentiate between geometrical distortions that do not alter image parallax relations and those that do. The former, which are introduced by such factors as misalignment of the film projector with respect to the digitizing camera, can be corrected using fiducial marks located in a single depth plane of the original scene. On the other hand, misalignment of the optical system used to record on film a three-dimensional scene is liable to produce geometrical changes that cannot be compensated by such a scheme.

In situations where the relative positions of camera and subject are difficult to control, such as large-scale experiments, it is necessary to introduce in the field of view markers at various distances from the camera and apply three-dimensional correction schemes. In the present work, where it was possible to accurately arrange the different components, the correctness of all geometrical relations could be ensured before the recording. The need for markers on several planes was then eliminated.

The prescribed alignments between the various elements of the optical system were performed in two steps. First, the mirror complex was aligned with respect to the test section of the flow channel. Second, the high-speed camera was aligned with respect to the rest of the equipment. For each step, a set of alignment rules was defined and a protocol developed.

Alignment of the test section with the mirror system was required so that fiducial marks located at the corners of the windows could be used

for later geometrical corrections. For a test segment of square cross section, the following two conditions had to be met:

- a) all the mirror surfaces and both windows must be perpendicular to a common plane, referred to as the x-y plane, and
- b) the axis of symmetry of the mirror system must be a diagonal of the test section.

To achieve condition a), a plane perpendicular to the window surfaces was physically defined and used as a reference to align the mirror system. A sheet of light, obtained by placing a cylindrical lens in the path of a laser beam, was used for this purpose. The light sheet was shone onto the test section and oriented so that it met exactly a set of four co-planar fiducial marks around the perimeter of the flow channel. By this operation, the light sheet was made perpendicular to both window surfaces. The mirror system was then introduced in its intended position and a screen attached to it in front of the cut-out where the test section usually rested, requiring temporary removal of the flow channel. The cut-out allowed observation of the screen. If the light sheet was perpendicular to all the mirror surfaces, the projections from the right and left halves of the mirror system appeared as collinear, overlapping segments. Once this alignment was achieved, the test channel was returned to its original position. In applications where the flow tube could not be easily moved, the mirror complex might be translated in a self-parallel fashion on an optical rail mount.

Condition b), which insured that the optical axes for the two views

impinged symmetrically and perpendicularly in the x-y plane on the respective windows, was achieved mechanically by means of a template mounted under the bottom of the mirror box. The template was previously adjusted in tilt and forward position to be aligned with the axis of the box and keep the test section at the proper distance. When the flow channel and the mirror complex were brought together, either component could be rotated and/or translated in the x-y plane until the template matched the frontal corner of the test section. The simplicity of the operation, and also the advantage of being able to preset the distance between windows and mirror surfaces in a repeatable fashion, made this technique preferable over optical methods.

The optical axis of the high speed camera was aligned with the rest of the system according to the following rules:

- a) it must be parallel to the axis of symmetry of the mirror system;
- b) it must be contained in the plane of symmetry of the mirror system perpendicular to the x-y plane, and
- c) its z position (that is, measured orthogonal to the x-y plane) must be at the centerline of the windows.

To fulfill condition a), a laser beam was again used as reference. Without altering the alignments set in the previous phase, a mirror was attached to the frame of the mirror box facing the camera. The supporting structure of the box held the mirror perpendicular to the axis of symmetry of the orthogonal-view system. With the camera temporarily set aside, the unexpanded beam was shone onto the mirror and adjusted

until the incident and reflected rays coincided. The alignment mirror was then removed and the camera was placed at the proper distance from the rest of the optics, roughly on the correct line of sight. The image was framed in the viewfinder so that the two adjacent views filled the available area, with some border space being left to allow for edge cropping during projection. A mirror was attached to the back panel of the camera, which is perpendicular to the axis of the objective lens, so that it was struck by the laser beam. Proper alignment according to condition a) was obtained by swinging and/or tilting the camera on the tripod mount to bring the incident and reflected rays to overlap. By self-parallel translation and elevation of the camera, a crosshair at the center of the viewfinder was brought to coincide in one direction with the midline of the mirror box frame and in the other direction with the common midline of the adjacent window images. This satisfied conditions b) and c) respectively. In practice, since the camera could seldom be displaced quite parallel to itself, re-orientation of the axis and centering of the image had to be iterated until all conditions were met.

### 2.3 Image digitization

The process of turning visual information from an experiment into a digitized form understandable to a computer can be performed in several ways. The relatively high framing rates required in many flow visualization applications pose practical limits on some of the methods.

The most efficient path would be to link directly a fast-scan TV camera and controller system to a high-throughput analog-to-digital converter, capable of sampling all the image elements in a frame several hundred times a second. The speed requirements posed on such a system are considerable: for a good resolution, 400x400-element image, 160000 data conversions must be performed for each frame. Just to achieve framing rates of the order of 200 pictures per second, a 32 MHz data conversion rate is needed, a figure at the upper end of today's technological capabilities.

A hybrid system using high-speed analog video recording followed by video digitization of the recorded signal is the next choice. Here the burden of high framing rate processing is removed from the analog-to-digital converter, since the video tape can be adequately slowed down at playback. However, only very few video recording systems exist that allow framing rates higher than the customary 30 per second of ordinary television systems. In this field the market is currently dominated by the Kodak Spin Physics SP2000 motion analysis system. This remarkable unit can record at a maximum rate of 2000 images per second for one minute, and allows playback in standard NTSC (National Television System Committee) format with various built-in editing and processing features. The cost of such a system limits its attractiveness for many research applications.

A third solution, which uses more readily available technology, has been adopted in this work. The crucial task of high-speed visual data acquisition is performed using a fast conventional movie camera, an

instrument which - though sophisticated - is virtually standard equipment for most flow visualization applications. The processed film is then video digitized by projecting each frame in front of a TV camera connected to an analog to digital converter system. No speed requirements, other than those arising from practical convenience, are posed on the digitizing system. This allows the use of standard, moderate-cost devices using either vacuum tube or solid-state technology for the image pick-up. The high-speed movie camera used here was a HYCAM (Redlake Corporation, Santa Clara, Ca.), capable of regulated framing rates of up to 5000 pictures per second on 16-mm film. Excellent results in terms of image resolution and exposure speed are obtained using fast colour reversal film such as Kodak Ektachrome 7250, rated at 400 ASA. This film can be push-processed to a speed of 800 ASA without pronounced degradation in image quality.

The processed film was projected on a frosted-glass screen using a 16-mm projector (model 224-A, L-W Photo-Inc., Van Nuys, Ca.) capable of single frame advance. A video camera looking at the other side of the screen picked up the image to be digitized. The axes of projector and TV camera were approximately aligned with each other and normal to the screen. Geometric correction in the analysis software eliminated the need for precise alignment. After each frame advance the shutter had to be arrested in the fully open position. Some projectors, among them the 224-A, keep the shutter in motion when the film transport is stopped to maintain the apparent frame brightness constant, with the result that parts of the picture that happen to be sampled when the

shutter is closed will appear black in the digitized picture.

The video digitizer system consisted of a HAMAMATSU Vidicon camera and C1000 controller, connected to a Digital Equipment Corporation LSI-11/23 system. The image sampling software makes use of a pre-written FORTRAN subroutine package running under the RT-11 operating system. The data transfer between the controller and the computer was performed using Direct Memory Access (DMA), thus minimizing overhead time. The digitizer was capable of resolving 1024x1024 image elements (pixels) in a full frame, but the time required for a scan at this resolution is almost seven minutes. At a resolution of 512x512 pixels per full frame, which is customary for many image processing applications, the scan time is slightly over one and a half minutes. More modern 'slow' image acquisition units such as the solid-state EIKONIX EC 78/99 would reduce this time to a matter of a few seconds. Each sampled picture element was converted in the HAMAMATSU system to an integer between 0 and 255, hence allowing a maximum of 256 shades of grey to be differentiated. The width of the useful frame area on 16 mm film shot with the HYCAM is 10 mm. Assuming that the width of the projected frame spans the entire video field, the spatial resolution at the film plane is 19.5  $\mu\text{m}$  in the 512x512-pixel mode. While limited compared to the resolving power of the film itself, this pixel size was sufficiently fine to reveal accurately the tracer images. The scanned field could be cropped on any side if the area to be analyzed did not occupy the entire video field, and the digitization time was reduced in proportion.

The digitized images were temporarily stored on an RL01 hard disk unit on the LSI-11 system. The intensity values for each image were organized as an unformatted direct-access file. A subsidiary formatted header file contained information such as the dimensions in pixels of the image in the corresponding data file and optional comments on its nature. The size information in the header file was necessary so that other software could reconstruct the record length of the data file (which is related to the height of the scanned field). The files were transferred off-line, using floppy disks, to a VAX 11/750 system for analysis.

## CHAPTER 3

### IMAGE ANALYSIS

#### 3.1 Introduction

A digitized image, however obtained, is a matrix of intensity values. The  $(i,j)$ -th element is a number that depends, usually in a linear fashion, on the brightness of the image at the intersection of the  $i$ -th row and the  $j$ -th column of pixels, which are discrete image elements arranged in a regular grid. The range of values that the elements can assume depends on the precision to which the conversion from intensity, or an analog electric signal proportional to it, to numeric form has been performed. If the analog-to-digital converter has a precision of eight bits, the highest intensity value (white) will be represented by the number 255 ( $2^8-1$ , or 11111111 in binary), while 0 always represents black.

The intensity matrix can be manipulated in a variety of ways, which result in changes to the image it represents. Alterations may be made both to the order of the elements and their values.

Re-ordering of the matrix elements produces geometrical changes of varying degrees of complexity in the image. For example, if the image is described by an  $n \times m$  matrix  $F$ , a new matrix  $F'$  obtained by  $f'_{i,j} = f_{i,m+1-j}$  describes a right-left inverted image. This transformation amounts to multiplying the original matrix  $F$  by an  $m \times m$  matrix  $A$  given by  $a_{i,j} = \delta_{m+1-i,j}$ .

Much more useful in the field of image processing are matrix operations that leave the image geometrically unchanged but modify the intensity distribution to augment selected features. Depending on their effect on the image, various manipulations go by the name of contrast enhancement, edge enhancement, frequency filtering and so on. Some of these operations affect the value of one pixel independently of those of its neighbors, and are therefore called point-dependent processes. Other operations, known as region-dependent processes, use the original values in a prescribed neighborhood of a given pixel to determine the new value at that pixel. Many contrast enhancement techniques fall into the first category, whereas edge enhancement and filtering methods are usually of the second type.

A picture that has been enhanced or manipulated as previously mentioned still constitutes a single image space, although to a human observer it may appear to be composed of well defined regions such as a figure and a background, in the simplest case. To emulate on a machine - at least partially - the human perception of an image, the regions of interest must be extracted from the intensity matrix. The term 'segmentation' is used to denote any process whereby the image space is partitioned into regions that are meaningful for the particular application involved. For certain image recognition procedures this is a very complex task, in which a wide array of visual characteristics of objects to be identified must be taken into account. For other applications, much simpler criteria are adequate. Depending on the situation, the segmentation problem can best be approached as a

point- or a region-dependent process.

A typical machine vision application, at any level of complexity, usually requires a combination of image enhancement, for instance, to bring out by digital filtering details buried in noise, and image segmentation. The many techniques that are available to perform these tasks are discussed at length in the books by Gonzalez and Wintz (1977) and Hall (1979). The selection of the most appropriate methods for a given situation must often be carried out by successive trials, although the nature of the images to be analyzed may indicate a particular approach to the problem.

For the purpose of the present work, a relatively simple distinction between figure and ground was required to identify the images of tracers against a contrasting background. Problems to be overcome when analyzing the images were limited intensity range, that is, poor contrast, and non-uniform luminosity of background and tracers. In the following sections, techniques of image enhancement and segmentation that were considered in connection with this work are described, and the reasons behind the choice of a particular method or combination of methods are discussed.

### 3.2 Image enhancement by histogram modification

In an actual digitized image, the intensity values represented in the matrix do not usually span the entire available range (0 to N). An image with low contrast may have an intensity distribution concentrated

in a narrow interval  $(m_1, m_2)$  of the available range (figure 4a). One of the simplest methods of increasing the contrast of such an image, and hence its discernibility, is a linear scaling transformation that 'normalizes' the actual intensity values so that they are distributed over the entire range (figure 4b). In terms of matrices, this scaling is obtained by adding to  $F$  an  $n \times m$  matrix  $A$  given by  $a_{i,j} = -m_1$  and multiplying the result by a scalar  $c = N/(m_2 - m_1)$ . It may be argued that this type of contrast enhancement is inconsequential for anything but direct observation of the restituted image, since it does not affect in any way the statistical distribution of values. It is nevertheless a useful form of preprocessing when analyzing common features in image sequences, since it removes frame-to-frame discrepancies due to changes in overall lighting level or detector response. A problem which is intrinsic to any manipulation that alters the intensity range arises from the fact that the distribution is quantized in the first place. The limited-range input histogram only contains a fraction of all the possible distinct intensity values, and the output of the transfer function will contain the same number of separate values, only spread over a wider range. The result is a coarse quantization, which does not use all the grey levels available and hence leaves gaps in the histogram. The problem can be minimized by an analog operation of amplifier gain and offset on the input signal before it is quantized by the analog-to-digital converter, so that the raw digital data will cover as nearly as possible the entire available range. Another approach would be to convert the input signal to digital form with a

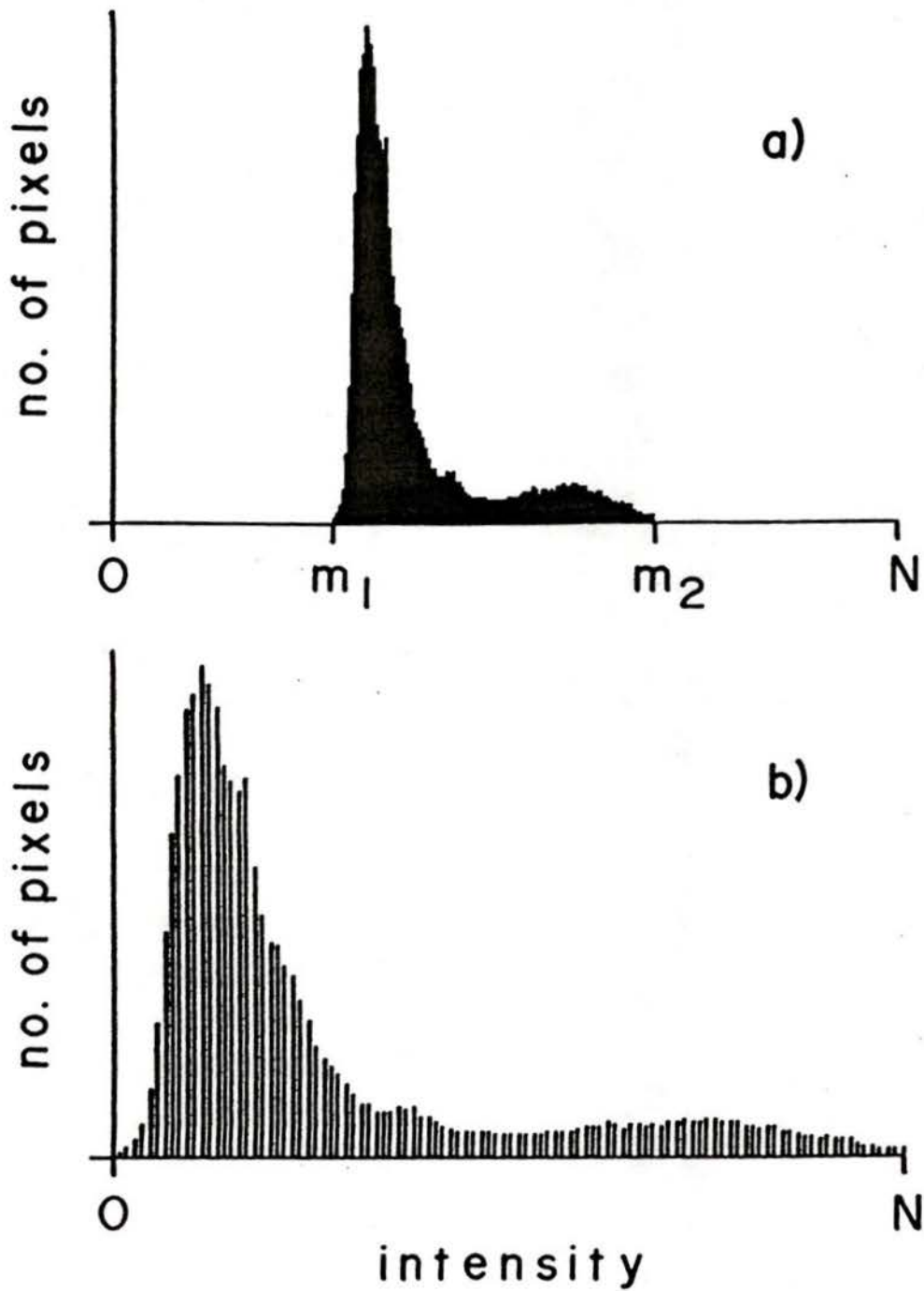


Figure 4. Example of intensity histogram of a digitized image: a) original histogram; b) histogram expanded over the entire available intensity range.

higher resolution than will eventually be used, say 10 bits versus 8 bits. If the input distribution spans 256 or more of the 1024 separate grey levels available at 10 bits, then scaling of the digital data and re-quantization at 8 bits will represent each grey level in the correct proportion.

Non-linear mappings between input and output intensity values can be useful for some applications. An important example is the logarithmic transformation, which usually provides a more equal distribution of grey levels and makes low-contrast detail more visible by enhancing low-contrast edges. Some scanning equipment has the option of performing such log mapping by means of an operational amplifier with a transistor in the feedback loop. The logarithmic transform generally expands a peaky input probability distribution into a broader output distribution.

The concept of transforming the image probability function in a systematic manner can be extended into the methods of histogram equalization and histogram specification. Histogram equalization is obtained by using a transfer function that maps each grey level into the cumulative distribution of all intensity values from zero to the level in question, multiplied by the maximum grey level value available. It can be shown (Gonzalez and Wintz, 1977) that for a continuous grey level distribution this gives a uniform probability density function over the entire intensity range. This can enhance low-intensity detail in a predominantly dark scene that also contains bright areas, whereas a linear scaling transformation would hardly affect such an image. For a

discrete distribution one seldom obtains a perfectly flat result, that is, an intensity histogram in which each grey level has the same pixel count. Nevertheless, the transformed image usually shows considerable improvement in contrast and detail. A note of caution applies to this technique: the number of distinct grey levels represented in the output image can at best be equal to that in the input image, and will be smaller if different intensity levels are mapped into the same output level. The previously discussed problem of coarse quantization should a fortiori be considered here.

Histogram equalization is a rigid mapping scheme, which does not allow any form of control over the final effect. Much more versatile, particularly in an interactive mode, is the technique known as histogram specification. As the name implies, this mapping transforms the original intensity histogram into one having a prescribed distribution. The underlying concept is that if the original histogram is equalized by transformation  $T$  and the prescribed histogram by transformation  $G$ , then the combined transformation  $G^{-1}(T)$  will map the original histogram into the prescribed one. The argument is rigorous only for continuous distributions, for which the equalization is exact. As shown in Gonzalez and Wintz (1977), however, it is easily applied in approximate form to discrete histograms, with the added advantage that the combined mapping can be specified point by point without the need to obtain  $G^{-1}$  analytically. Beside expanding the dynamic range, histogram specification allows the histogram to be biased toward certain sections of the spectrum to better control the contrast of the output image at specific

intensity levels.

After various methods were tried, the linear scaling transformation was eventually adopted. It was discovered that methods such as histogram equalization were detrimental to the type of figure-ground analysis to be performed here, because of the tendency to enhance unnecessary detail in the low-intensity background. The logarithmic transform had the same effect. Although direct histogram specification could in principle be tailored to increase the tonal separation between tracers and background, it would have required optimization of the shape of the prescribed distribution for each new series of images. It appeared more convenient to apply simple linear scaling to the original histogram and rely on a more sophisticated segmentation criterion, based on gradient as well as intensity, to distinguish the tracers.

### 3.3 Image segmentation

The type of scene to be analyzed in this study could be considered as a binary system consisting only of the figure, i.e. the flow tracers, and the background. Since no other differentiation was required, the image matrix could be reduced from a set of multiple-bit values to a bit-map, in which each element could assume only the values 0 or 1. The task of the image segmentation step was therefore to assign the value 1 to 'figure' pixels and 0 to 'ground' pixels. Since the background was dark, while the objects to be recognized were bright, those pixels with intensity values above a given threshold could be mapped as

'1' and the others as '0'. If the intensity function  $I(x,y)$  of an image in the  $x$ - $y$  plane is plotted as a surface in the space  $(x,y,I)$ , the method can be interpreted as 'slicing' that surface with a plane parallel to the co-ordinate plane of the image, and is therefore known as 'intensity slicing'. Alternatively, the method may be seen as a unit step transformation operating on the grey levels of the intensity matrix. The setting of the threshold level at which the step occurs is crucial for the accuracy of image interpretation.

In an optimal situation, dark pixels from the background and bright pixels from the figure would form well separated peaks in the intensity distribution (figure 5a), with a trough between them where the probability function is almost zero. The location of the threshold within that low-probability interval would not be critical, since any error in interpretation would be limited to relatively few pixels. Unfortunately, the intensity distribution of most images analyzed did not reflect the optimal situation. In most cases, the bright pixels did not form an isolated, easily identifiable peak in the intensity spectrum. The histogram was similar to that shown in figure 5b, with a pronounced peak in the dark section of the spectrum that gradually decreased into a broad, low distribution at the bright end. The luminosity of background pixels and object pixels varied in different areas of the field, causing a broadening of the peaks and substantial overlapping of the contributions to the spectrum from each population. Under these conditions, a point-dependent process such as intensity slicing was useless in differentiating between the two groups.

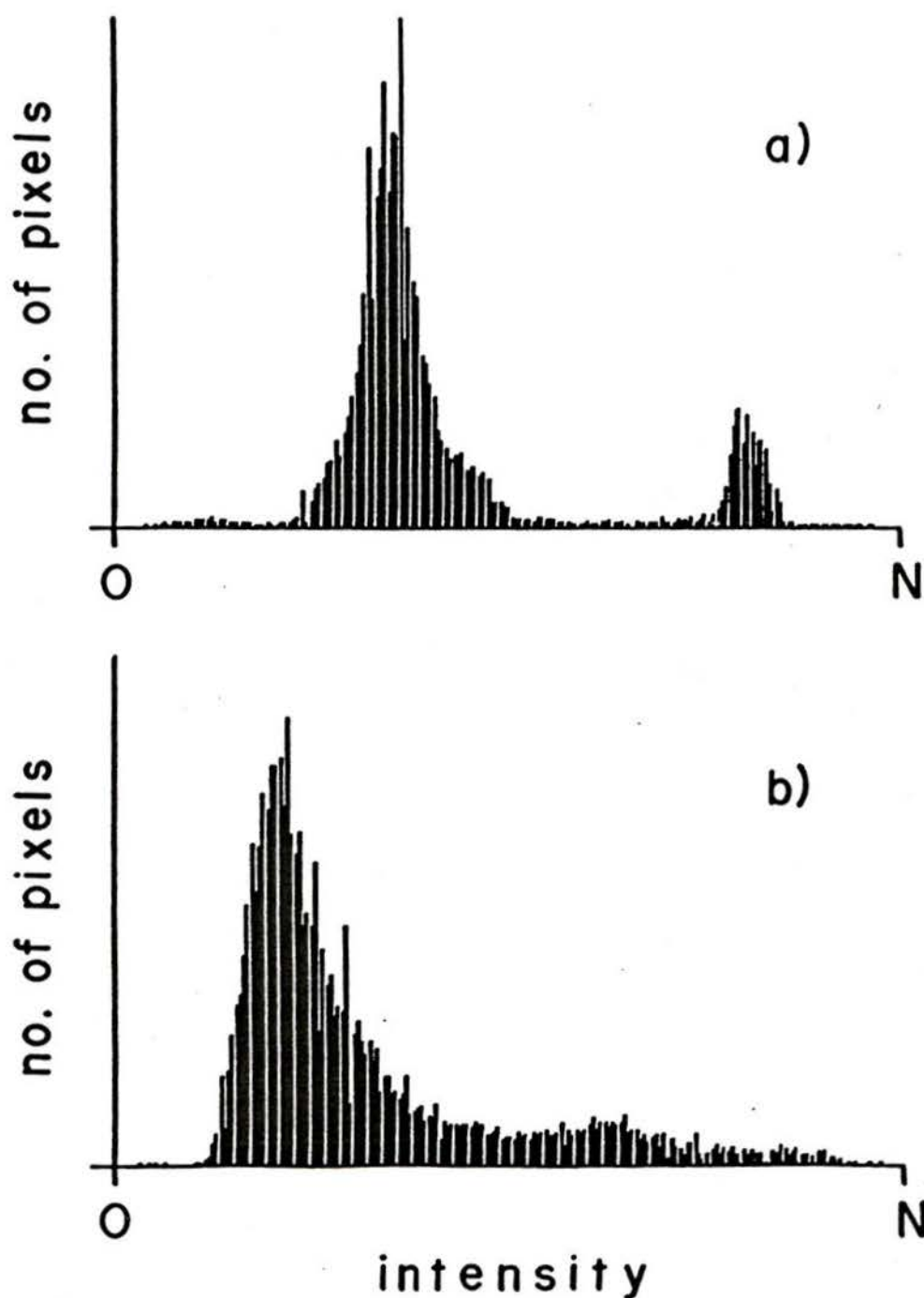


Figure 5. Examples of intensity histograms of digitized images: a) ideal situation, with well defined peaks from dark and bright areas of the scene; b) poorly defined peaks due to spread in the intensity values. Both histograms are expanded to full range.

Region-dependent processes, on the other hand, could be used to locate the boundaries of bright features, which were usually well discernible in contrast with the intensity of the local background. Use could be made of the fact that the edges of objects give relatively sharp discontinuities in the intensity level, which do not usually occur in the background itself even though its brightness may vary fairly widely from area to area. Template matching is a useful method for such segmentation applications. A template is an array designed to detect some local property of a region. The elements of a template are the averaging weights to be applied to the corresponding pixel intensities.

Consider a template of the form

|       |       |       |
|-------|-------|-------|
| $w_1$ | $w_2$ | $w_3$ |
| $w_4$ | $w_5$ | $w_6$ |
| $w_7$ | $w_8$ | $w_9$ |

and let  $x_1, x_2, \dots, x_9$  be the corresponding pixels in a 3x3 region of the image to which the template is applied. By taking the product  $WX$  of the matrices  $W = [w_1 \ w_2 \ \dots \ w_9]$  and  $X = [x_1 \ x_2 \ \dots \ x_9]^T$ , we obtain a value which, depending on the type of template used, is an indication of the presence of a certain feature at the central point of the region. We say that the feature has been detected if  $WX > t$ , where  $t$  is a specified threshold. Templates for the detection of features such as points, lines or edges are described by Gonzalez and Wintz (1977) and

Hall (1979). The two edge-detecting templates shown below were used in combination to form a two-dimensional edge detection function:

|   |   |    |
|---|---|----|
| 1 | 0 | -1 |
| 2 | 0 | -2 |
| 1 | 0 | -1 |

|    |    |    |
|----|----|----|
| -1 | -2 | -1 |
| 0  | 0  | 0  |
| 1  | 2  | 1  |

When applied to a given 3x3 region of an intensity matrix, centered at element (m,n), these templates yield the following approximate expressions for the local gradients in the x and y directions respectively:

$$d_x = (f_{m-1,n-1} + 2f_{m,n-1} + f_{m+1,n-1}) - (f_{m-1,n+1} + 2f_{m,n+1} + f_{m+1,n+1}), \quad (3.3.1)$$

$$d_y = (f_{m+1,n-1} + 2f_{m+1,n} + f_{m+1,n+1}) - (f_{m-1,n-1} + 2f_{m-1,n} + f_{m-1,n+1}). \quad (3.3.2)$$

The derivative magnitude at location (m,n) of the array is generally defined in terms of the local gradients as

$$S(m,n) = (d_x^2 + d_y^2)^{1/2}. \quad (3.3.3)$$

$S(m,n)$  is known as the Sobel operator for the  $d_x$  and  $d_y$  given by (3.3.1) and (3.3.2). This edge detection function was found to give a sharp response and to generate thresholded edges of good continuity for many types of image.

Best segmentation quality for the images used in this study was achieved through the combined use of intensity slicing and edge thresholding. At each point of the image the intensity was tested, and if above a specified threshold, the Sobel operator at that point was

computed and compared to another threshold. Only if both parameters were above the respective thresholds was the pixel coded as 1 in the bit-map. If the intensity threshold was set somewhat below the lowest expected intensity of features of interest, this scheme avoided the possibility that occasional sharp intensity transitions in the darker areas of the background would be registered as figure edges. It was found that an adequate setting for the intensity threshold of tracer images was usually near the centre of the intensity range. An added advantage of the combined method was that the time-consuming computation of the Sobel operator did not need to be performed on the pixels below the intensity threshold. For the typical grey level distribution of the images analyzed here, which was strongly biased toward the lower portion of the range, the saving in processing time was substantial. When implementing the Sobel operator formula, it was also more efficient to compute  $S^2(m,n)$ , without extracting the square root, and test this value against the square of the threshold.

Because of the need to have always available eight neighboring pixels for each image point being considered, the pixels at the boundary of the image field were not analyzed in the segmentation process. The thresholded bit-map is therefore two pixels narrower in both directions than the original image. The one-pixel boundary line was permanently set to all 0's.

Identified features consisting of a single pixel were found usually to be spurious. Even if they corresponded to very faint or blurred tracer images, they could not be reliably taken to represent the centre

of the feature. An optional processing step was therefore included that removed from the bit-map the '1' pixels with all eight neighbouring pixels equal to 0.

### 3.4 Location of tracer images

In the thresholded bit-map, bright elements were represented by clusters of 1's. The core of a cluster might or might not be composed of 1's, depending on the uniformity of the brightness of the specific feature. Objects that had a very uniform luminosity level in the original image appeared as empty outlines because of the use of gradient thresholding, whereas objects of less uniform brightness might appear 'filled' to varying degrees. To locate the centroid of a feature, independently of internal pixel distribution, only the thin line of pixels that defined the outer boundary of the segmented region was used.

A contouring procedure commonly used in image encoding to describe the outer edge of a specific luminance region (Gonzalez and Wintz, 1977) was adopted here with some modifications. Starting at a '1' pixel, the algorithm traced the outer boundary of the largest connected set of '1' pixels, always terminating at the initial point. To locate a starting point, the bit-map matrix was scanned by columns until a 1 was found. The direction of travel from this, and all successive points within that contour, was decided using the following rule:

Define the most recent direction of travel as pointing north (N). Look at the neighbouring element in direction SW; if this element is a 1 move to it; if not, look to the neighbour in direction W; if it is a 1 move to it; if not, look in direction NW and so on. If a 1 is not found in any other direction, move to the neighbour in direction S, that is, the one whence the current point was entered. In any case, stop if the point just entered is the initial point of the contour.

Note that except for isolated '1' pixels, which were usually eliminated, at least one neighbour of the current position is necessarily a 1. The boundary can therefore be followed all the way to the starting point, building a walk that encloses the segmented region. The averaged co-ordinates of the points on the contour give the position of the centroid. It was assumed that the centroid of a contour and that of the enclosed area coincided, since all shapes of interest were approximately point symmetrical. After the centroid had been located and stored, all the bit-map elements on and inside the contour were changed to 0's so that they would not be reprocessed. Scanning along columns then resumed until the next cluster was located or the whole matrix had been examined. Since the flow tracers in this study had a typical size, it was possible to instruct the procedure to discard the contours whose length was more than a given maximum, thus removing from the scene extraneous features that might exist within the field of view.

The usual implementation of the algorithm for image encoding considers only neighbours on the same row or column, in order to reduce the number of possible directional codes to be stored or transmitted and

hence the required word length. The choice of making all eight neighbours of a point available as targets for the next step, thus allowing contour lines to proceed diagonally as well as by rows or columns, typically resulted in shorter, less ragged contours. This usually compensated for the extra execution time required to find a neighbouring '1' due to the larger number of possible look-up steps.

The contouring algorithm works best with segmented regions having well connected outlines. If gaps occur in the distribution of '1' elements around the outline, the algorithm may follow the boundary inside the region in complex fashions. More extensive gaps may result in separate contours being built. Figure 6 shows how progressive deterioration of a region outline can lead to faulty contouring. In 6a, the region has a properly connected outline and a few internal points. The algorithm, proceeding as shown, correctly encloses the region. In 6b, one point on the outline (indicated by an x) has not been included in the region. The algorithm still finds a continuous boundary, but the shape is grossly different from the 'correct' outline and would lead to a sizeable displacement of the centroid from its proper position. In 6c, one more point (indicated by a second x) is dropped. This time the error is severe, since the algorithm builds a first contour on a portion of the region, processes it, then resumes scanning and builds a second contour on the remaining portion of the region. As a consequence, two centroids are found. This example reveals the effect that a poor segmentation, arising from improperly set thresholds, can have on the end result of the scene analysis.

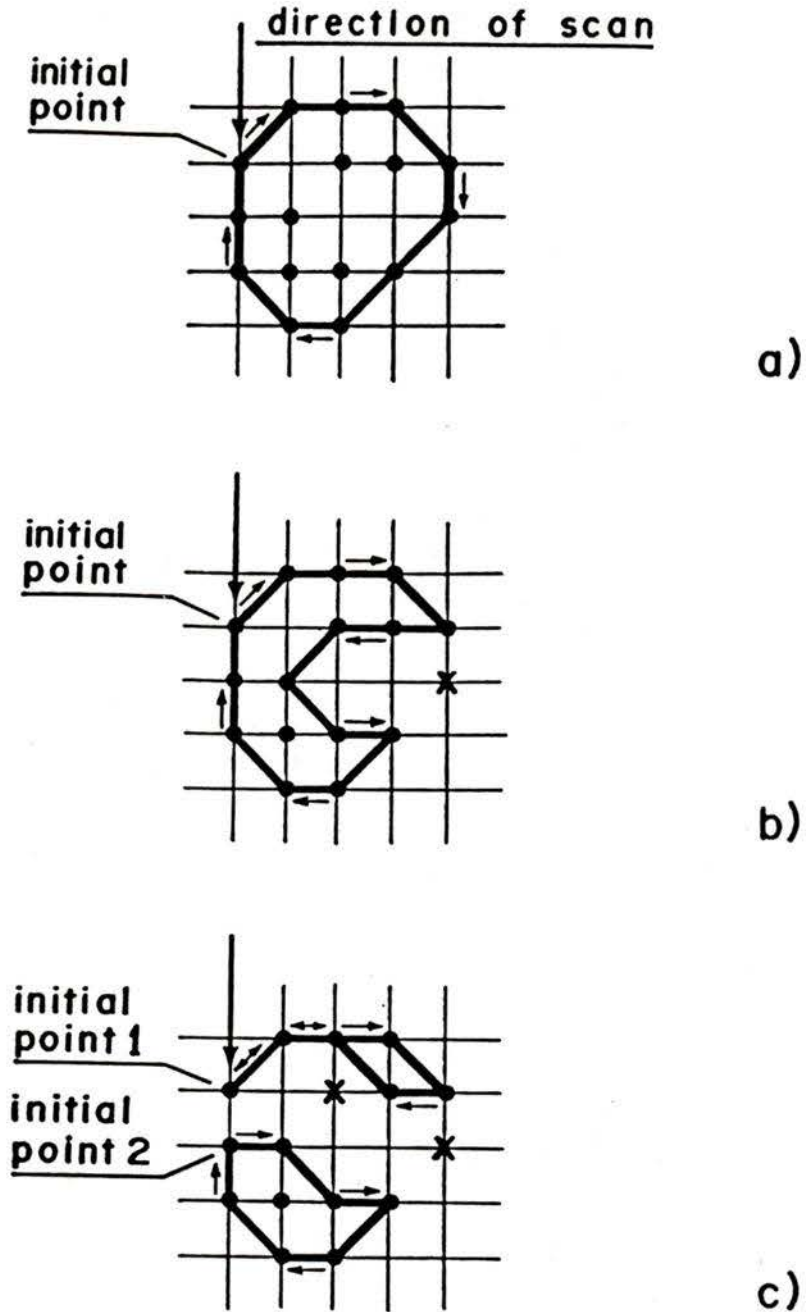


Figure 6. Demonstration of the effect of point drop-out on the contouring of a cluster of bright pixels: a) original condition; b) one point removed; c) two points removed, causing the contour to split.

### 3.5 Image processing equipment and procedure

The entire scene analysis process, starting from the digitized intensity matrix and culminating in a list of the centroid co-ordinates of selected image features, was performed on a VAX 11/750 system. An International Imaging Systems (I<sup>2</sup>S) model 70 image processor and workstation served as human interface in the interactive steps such as threshold specification. The grey-scale image, after intensity range expansion, was displayed on the workstation screen (figure 7a). The user could specify the desired thresholds for intensity slicing and edge detection, after which the segmented bit-map was computed and overlaid in color on the original image (figure 7b). If the quality of the segmentation was not satisfactory, the thresholds could be modified. Once an acceptable result was achieved, the region contours and centroid locations were determined and overlaid in colors on the original image, replacing the bit-map overlay (figure 7c). Again at this stage it was possible to go back to the specification of thresholds if the end result revealed inadequacies in the segmentation. The thresholds selected for the first frame in a sequence could be applied to all the remaining images without re-adjustment.

Despite careful specification of the parameters for segmentation, some particularly low-quality images still lead to faulty location of centroids in the ways described at the end of the previous section. The user therefore had the option, upon examination of the centroid positions, to invoke a special-purpose, trackball-driven graphics edi-

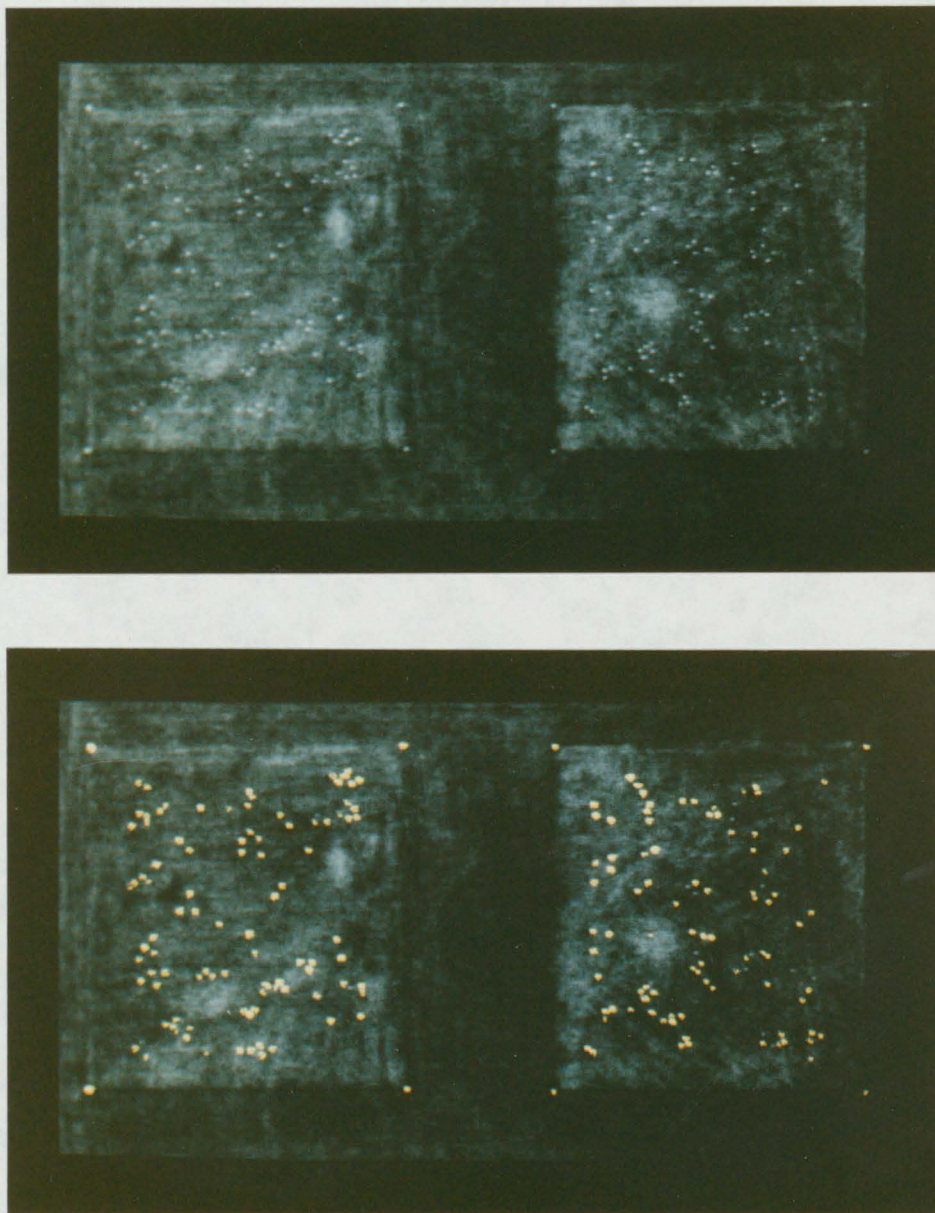
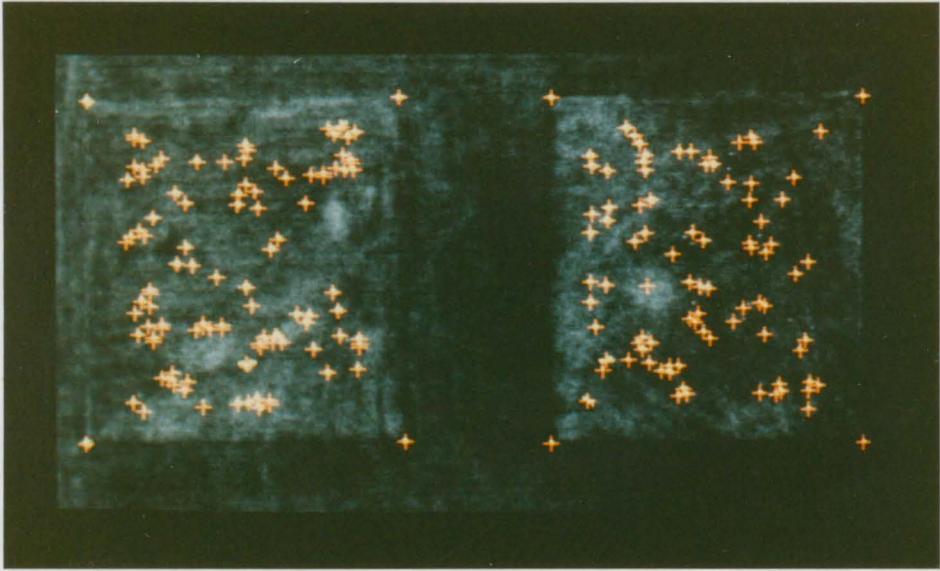


Figure 7. Typical image analysis sequence: a) original image, range-expanded; b) bit-map from segmentation overlaid on image;



c) centroids of tracers located and overlaid on image.

tor to perform manual adjustments. Most available functions were region-oriented, that is, they operated on all the centroids included in an interactively defined area. These included deletion of unwanted centroids and averaging of selected centroids into a single one. The latter operation was often effective when a feature of interest was split by the segmentation process into similarly-sized fragments. The only point-oriented function was addition of a centroid at any desired location. All changes performed graphically on the screen were reflected in the list of stored co-ordinates. An example of the operation of the editor to delete a wrongly identified centroid is shown in the sequence of figures 8a,b,c. For images of reasonable quality, manual editing was very seldom required.

The last step of the image analysis process was the identification of eight of the located centroids as fiducial marks. The operation was performed automatically, using the fact that the fiducial marks were located at the corners of the windows, and therefore appeared on the edges of the two separate sets of centroids. The user could change interactively the identification if the procedure's heuristics selected the wrong points, but this facility was never required in normal circumstances.

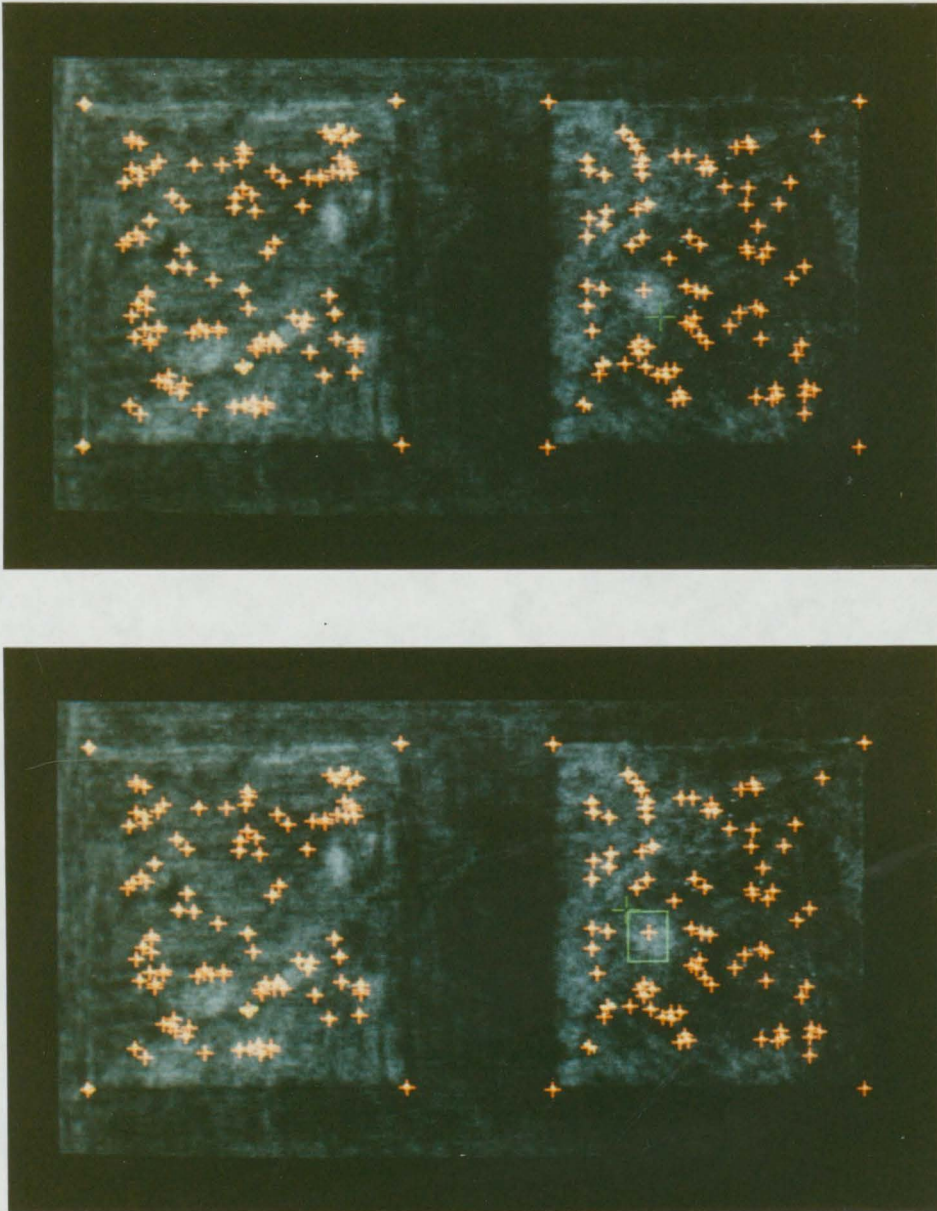
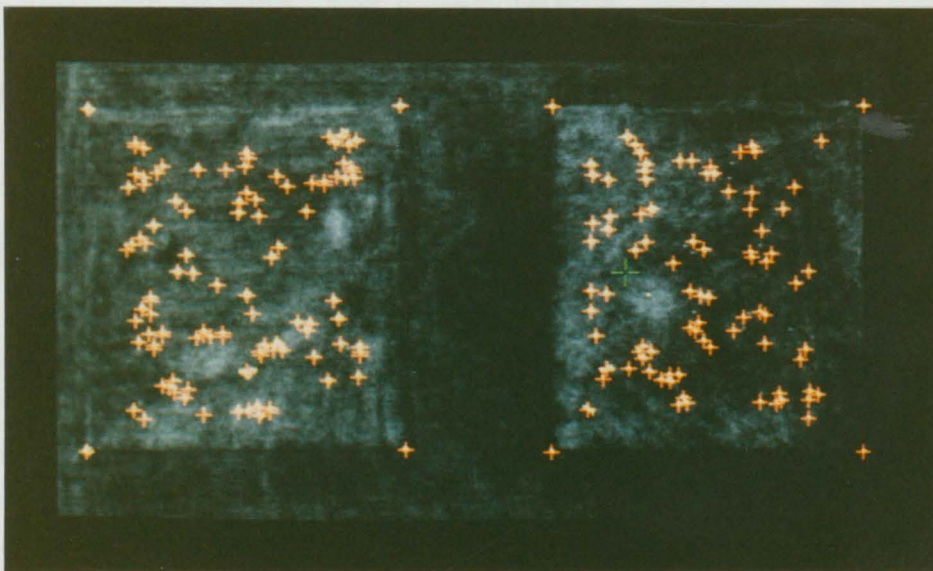


Figure 8. Example of interactive editing of image data: a) the cursor is placed near a wrongly identified centroid; b) an area of action enclosing the centroid is defined;



c) the centroid enclosed in the area is deleted.

## CHAPTER 4

### TRACER MOTION ANALYSIS

#### 4.1 Matching of pairs

Once the centres of tracer images had been located in the perpendicular views, they were correlated to give the spatial location of the tracers. Two images, one in each view, that correspond to the same point in space will henceforth be referred to as an 'orthogonal pair', after the term 'stereo pair' used to indicate corresponding points in stereo photography.

The identification of orthogonal pairs was based solely on geometrical considerations, without resorting to factors such as similarity in brightness and apparent size and shape of the tracer images. These parameters, which can be very helpful in the matching of stereo pairs, are unreliable with perpendicular images, because the distances and angular relations between light source, tracer and camera - which influence size and brightness - can differ substantially in the two views.

A preliminary phase to the actual matching was the correction of linear distortions which may have been introduced during image digitization, for example, by lack of alignment between the projector and the video camera. Fiducial markers located on the flow channel at the four corners of each window were digitized along with the tracer images, allowing later correction of distortions in the image plane. However,

this correction could not compensate for lack of alignment during the photographing of the three-dimensional object, which introduces deviations from the assumed parallax relations.

The geometrical correction based on the fiducial markers took care of scaling, rotating and linearly reshaping each viewfield to bring its corners to coincide with their intended position. It may be thought of as a 'rubber sheet' transformation specified by the prescribed displacement of four points on the plane. For every point within the viewfield, the geometrical correction algorithm computed the new position in the rectified figure. The details of the transformation are given in appendix A.

Non-linear distortions, such as pincushion effect, are not corrected by a transformation based only on the corner points, but in this work such distortions were found to be negligible. If required, however, they could have been partially rectified by the same linear correction scheme presented above if more points along the perimeter of the viewfield had been considered. Several fiducial markers could be placed along the borders of the windows at regular distances, and the transformation applied to each quadrilateral section included between opposite pairs of adjacent markers. The correction would be performed in two passes, first considering markers along one pair of opposite sides and then along the other pair. More complex aberrations of the field of view, however, could only be rectified if fiducial markers were distributed throughout the visible area so that the transformation could be applied locally.

Once each view had been rectified to its correct proportions, the process of matching corresponding points was begun. In the absence of parallax, orthogonal pairs would have identical position in the direction common to both views. This condition is approximated by using a camera lens of long focal length and increasing the distance between camera and subject, as in Peskin's (1972) work. More accurate results are obtained by applying parallax correction, which requires forming tentative matches between likely orthogonal pairs and verifying their validity on the basis of the restituted three-dimensional co-ordinates. The distance between camera and subject is then unrestricted.

Figure 9 shows an x-y section of the orthogonal-view optical system. The dashed line represents the optical axis of the camera, which is deflected by the mirrors along two different paths. Picture planes, that is, planes on which the virtual image of each view is considered, are located at a distance  $D$  from the common viewpoint  $V$ , measured along the optical paths. Each plane is perpendicular to the corresponding optical axis. The intersection of the picture planes defines the  $z$  axis of a co-ordinate system, and the  $x$  and  $y$  axes are oriented to lie within these planes. The origin is set at an arbitrary position in the  $z$  direction. With respect to this origin, the optical axes are described by the lines  $(x = d_a, z = z_a)$  and  $(y = d_a, z = z_a)$ . Instead of following the actual optical paths going through the mirror system to a single viewpoint, one can consider straight optical axes along the lines given above and separate virtual viewpoints  $V'$ ,  $V''$  a distance  $D$  from the respective picture planes. A point at position  $(x,y,z)$  in the

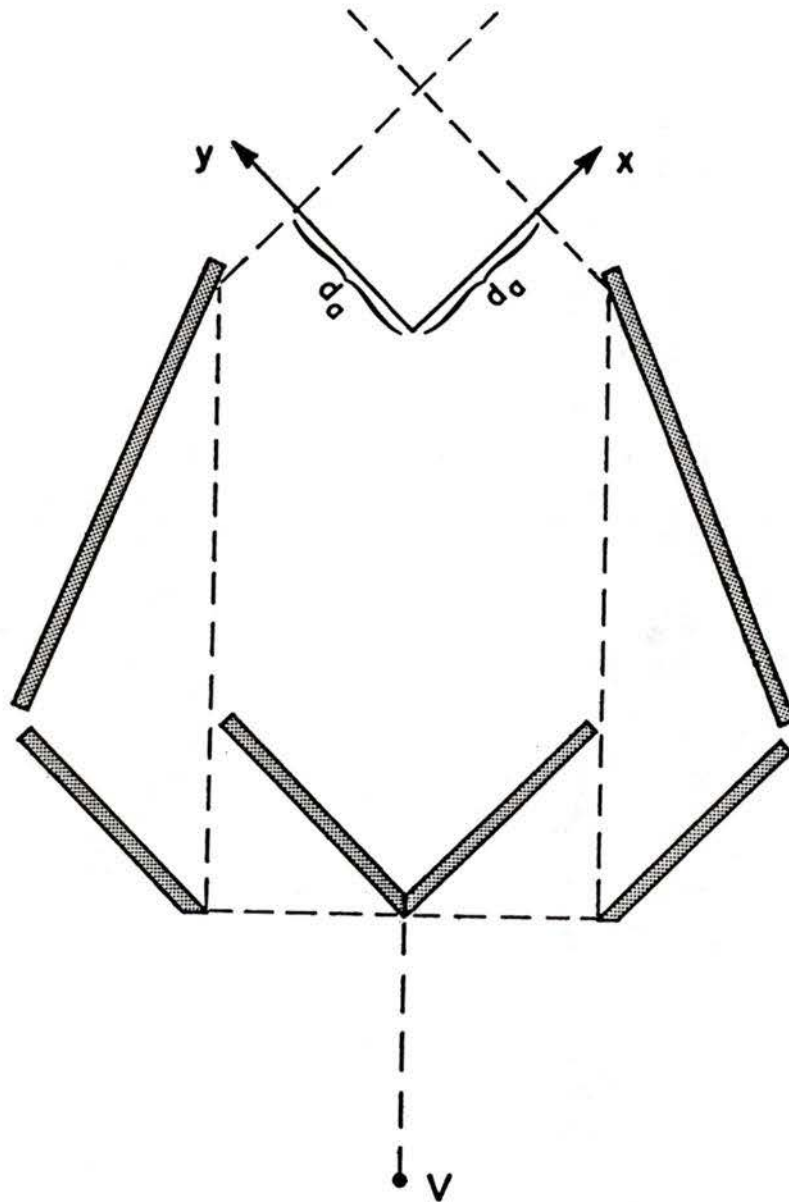


Figure 9. Diagram of orthogonal-view optical system, showing location of optical axes (dashed lines) relative to assigned cartesian axes.  $V$  is the viewpoint.

field of view will be seen along specific lines of sight from the two viewpoints. The intersection of a line of sight with the respective picture plane gives the position of the point's image on that plane. From the positions  $(x', z')$  on the plane  $y = 0$  and  $(y'', z'')$  on the plane  $x = 0$  the co-ordinates  $(x, y, z)$  can be uniquely reconstructed by the following relations, derived in Appendix B:

$$x = \frac{D^2 x' + D y'' (x' - d_a)}{D^2 - (y'' - d_a)(x' - d_a)} \quad (4.1.1)$$

$$y = \frac{D^2 y'' + D x' (y'' - d_a)}{D^2 - (y'' - d_a)(x' - d_a)} \quad (4.1.2)$$

$$z = z' + \frac{D y'' + x' (y'' - d_a)}{D^2 - (y'' - d_a)(x' - d_a)} (z' - z_a) \quad (4.1.3a)$$

$$z = z'' + \frac{D x' + y'' (x' - d_a)}{D^2 - (y'' - d_a)(x' - d_a)} (z'' - z_a) \quad (4.1.3b)$$

The availability of two independent expressions for  $z$ , which is a direct consequence of the fact that the  $z$  axis is common to both views, was the basis of the selection criterion for points that formed orthogonal pairs. The two values for  $z$  will be identical if and only if the projected co-ordinates  $x', z', y'', z''$  identify an orthogonal pair. The criterion can therefore be used to verify whether two image points, tentatively matched, do form an acceptable pair. Situations exist, however, in which two image points that pass this test do not correspond to the same real object point, but rather reconstruct the position of a fictitious point. Figure 10 gives an example of such a

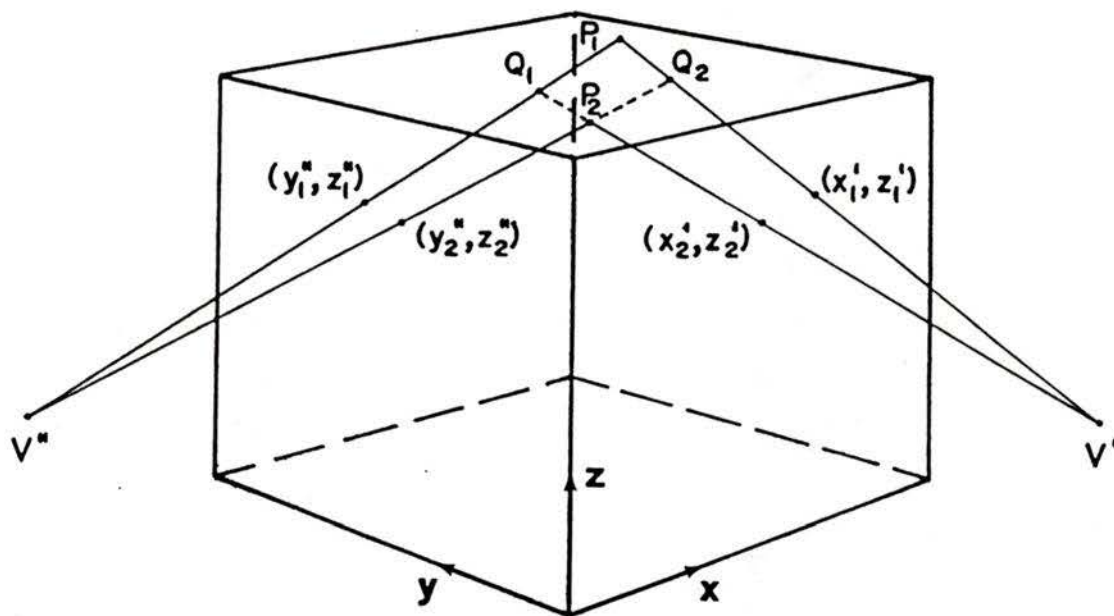


Figure 10. Example of matching ambiguity for points coplanar with both virtual viewpoints.  $P_1, P_2$  are real points;  $Q_1, Q_2$  are fictitious points reconstructed by matching the wrong pairs of images in the two views.

condition. Points  $P_1$  and  $P_2$  are real object points; their projected positions in the two views are  $\{(x_1', z_1'), (y_1'', z_1'')\}$  and  $\{(x_2', z_2'), (y_2'', z_2'')\}$  respectively. However, if image points  $(x_2', z_2')$  and  $(y_1'', z_1'')$  are matched they reconstruct the spatial position of the fictitious point  $Q_1$ , while the remaining two image points give the co-ordinates of  $Q_2$ , also fictitious. In both cases the  $z$  values from the independent equations agree. This ambiguity, which is not resolvable with only two views, occurs whenever two object points are coplanar with both virtual viewpoints.

Although the selection criterion based on the parallax correction equations is not infallible, as has just been shown, it is nevertheless useful inasmuch as it rules out pairs of images that couldn't possibly correspond to a single object point. With rare exceptions, in practical situations the remaining matches will indeed represent orthogonal pairs from true points. It would be possible to resolve most ambiguities by using positional information from the previous or the following frame, because of the unlikelihood that the coplanarity condition will persist in more than one frame. However, the extra processing could hardly be justified in view of the rare occurrence of the condition in even one frame. Should an isolated mismatch occur, its consequences would usually be limited to a one-step break in one or at most two trajectories.

When dealing with actual conditions, in which some degree of error affects the measured positions of the image points, it could not be expected that the two computed  $z$  values would agree exactly when a

correct pair was processed using the reconstruction equations. A small tolerance was allowed so that only pairs beyond a reasonable limit were excluded. If for a given image point in one view there were several feasible matches in the other view, the match which gave the closest agreement in  $z$  values was selected. If the selected match was already taken, it was re-assigned to the new point if the resulting pair gave a better agreement of  $z$  values than the previous one. The point that remained unmatched was then tested against other candidates, if any, within the tolerance limit. The task of finding all matches in one set of orthogonal images was therefore a problem of creating as many disjoint pairs as possible for which the discrepancies in reconstructed  $z$  positions were minimum. Situations of compromise in which the mean discrepancy was minimized for a group of pairs were not sought, nor were image points in one view allowed to find more than one match each. This strategy was designed to reduce the chances of mismatches, at the expense of losing the occasional correct match in some situations - for instance if the images of two object points coincided in one view.

The matching procedure was optimized in several ways. First, for a given point in one view (view A) not all points in the other view (view B) need to be considered as possible matches and tested by the parallax correction equations. Image points in view B whose apparent  $z$  position differs from that of the point in view A by more than a certain limit cannot possibly form an orthogonal pair. Consider an observed volume having dimension  $W$ ,  $L$  and  $H$  in the  $x$ ,  $y$  and  $z$  directions respectively. Let the picture planes correspond to the surfaces of the viewfield

closest to the viewpoints, and let  $z_a = H/2$ . Without loss of generality, assume that  $W > L$ . Now consider an object point at  $(W, 0, z)$ , hence adjacent to the picture plane  $y = 0$  and as far away as possible from the plane  $x = 0$ . From equations (3) and (4) in Appendix B the projected  $z$  positions of this point on the picture planes will be

$$z' = z \quad \text{and} \quad z'' = \frac{H}{2} + \frac{D(z-H/2)}{D+W} .$$

The difference between  $z'$  and  $z''$  can be expressed as

$$\left(z - \frac{H}{2}\right) \left(1 - \frac{D}{D+W}\right) ,$$

whose absolute value is maximized - within the boundaries of the field of view - for  $z = 0$  or  $z = H$ . The maximum absolute difference

$$\tau = \frac{H}{2} \left(1 - \frac{D}{D+W}\right)$$

is in fact the largest possible discrepancy between  $z'$  and  $z''$  for an orthogonal pair corresponding to a point in the viewfield. Hence the parallax correction only needed to be attempted on pairs of image points for which  $|z' - z''| < \tau$ , greatly reducing the number of computations involved. It was also advantageous to sort the co-ordinate pairs of points in the view in which matches were sought in order of apparent  $z$  position. This allowed the search for a match to be stopped as soon as the discrepancy between  $z'$  and  $z''$  increased beyond  $\tau$ , since all the feasible matches had then been examined.

The matching procedure could also be streamlined in the handling of disputed matches. Consider an image point that had originally found a match but has been deprived of it because another point claimed the same match with a closer agreement of reconstructed  $z$  values. It may well happen that the second point will then move on to a better match as successive candidates are scanned, thus leaving the previous match free for the other point to take back. For efficiency, the identity of the previous owner of the match was stored aside when the match was claimed away from it, so that the restitution could be performed immediately with no need for the old owner to be run through the search again. This process of claiming and restitution of matches continued until the best match for the new point had been found. If this match was taken away from another point, the latter needed to go through a new search cycle to seek an alternative match. Eventually all points in one view were either matched or necessarily matchless for lack of suitable, available candidates. Since all disputes were decided on the basis of agreement between the two independently reconstructed  $z$  values, each matched pair had an associated variable containing the discrepancy between these values - in a sense, a measure of the reliability of that match. If the match was challenged, the current accuracy could simply be looked up rather than having to be recomputed.

At the end of the matching process the reconstructed spatial coordinates from all accepted orthogonal pairs were output. The  $z$  co-ordinate of each object point was taken as the average of the two independent values from the parallax correction equations.

## 4.2 Trajectory tracing

The method of tracking the trajectories of tracers used in this work is conceptually similar to the technique used by Chang and Tatterson (1983) to follow tracers in stereo views, inasmuch as both methods are based on the assumption that from one frame interval to the next the velocity vector of a given tracer will not change drastically. The two approaches, however, differ in the way information from the two views is utilized and continuing trajectories are identified.

Chang and Tatterson performed separate, two-dimensional tracking of tracer images in each stereo view, and later associated similar trajectories in the two views. Their method for extending a trajectory in one view involved building a table of slope and displacement values for all possible paths from a given point to points in the next frame within a certain range from it, and a similar table for the possible paths from each of these points to nearby points one frame further. Comparison of values in the two tables allowed consecutive steps to be selected that minimized the change in both slope and magnitude. The process could always review its most recent step if no further path could be found that matched its parameters.

In the present work, tracer positions obtained from the matching of orthogonal pairs were tracked in three-dimensional space. Working with tri-dimensional locations had the advantage of eliminating the possibility of two trajectories overlapping, because the position of each tracer in space is inviolable. This avoided the tracking ambiguities

that can originate from overlapping trajectories in individual views. Moreover, the approach of tracking points in each view and using the similarity of trajectories as a matching criterion is not applicable to perpendicular views, since the same trajectory can appear quite different from the two viewpoints.

Under the assumption that the velocity vector of a tracer changed only gradually in successive framing intervals, linear extrapolation of the displacement in one time step was used as an approximation of the path in the next step. A spherical search range was built around the predicted position and the tracer locations in the next frame were scanned to seek unassigned tracers within the search range. If any were found, the trajectory was extended to the one nearest to the predicted position, and that tracer location was made unavailable to other trajectories. Otherwise, the tracer being followed was considered lost and the trajectory terminated.

Tracers for which no previous trajectories existed were handled in a different way, since a predicted trajectory step could not be constructed. The radius of the search range around the first position of a tracer was made as large as the maximum expected displacement per frame interval in the flow under study. More than one tracer position in the subsequent frame might be found within this relatively large search sphere. The tracer that was nearest to the original location was used as initial successor candidate. Only if the mean distance between tracers was large compared to the displacement between frames could the choice be accepted without verification. In general, how-

ever, it was impossible to decide which one of the positions within range was the proper successor on the basis of its displacement relative to the initial location. A candidate was verified by extending the search one frame further, using the tentative first step to predict the next position. If a successor could be found within the small search sphere constructed around the predicted position, the two-step trajectory was accepted. Otherwise, the process went back one frame and attempted to start a trajectory using the next nearest tracer in the second frame still within the initial search sphere. Attempts to follow a new tracer were given up if none of the trajectory starts could be continued into the third frame.

A graphical example of how a tracer was followed through four frames is presented in figure 11. The first appearance of the tracer is indicated by  $\bullet$ . A spherical range of radius  $r_1$  centered at this position is considered in the search for the first successor. Tracer positions in the next frame are denoted by  $\circ$  and identified by numbers. Positions 1, 2 and 3 fall within the search range. The nearest one to the initial position, number 1, is tentatively chosen as a successor. The predicted position in the third frame is linearly extrapolated based on the first step, and a spherical range of radius  $r_2$  is built around it. None of the tracer positions in the third frame, indicated by  $+$ , is found within the search range; the trajectory start is therefore abandoned. Tracer number 2 in the second frame, which is the second nearest to the initial position, is examined next. As before, the position in the third frame is predicted and a search radius  $r_2$  is

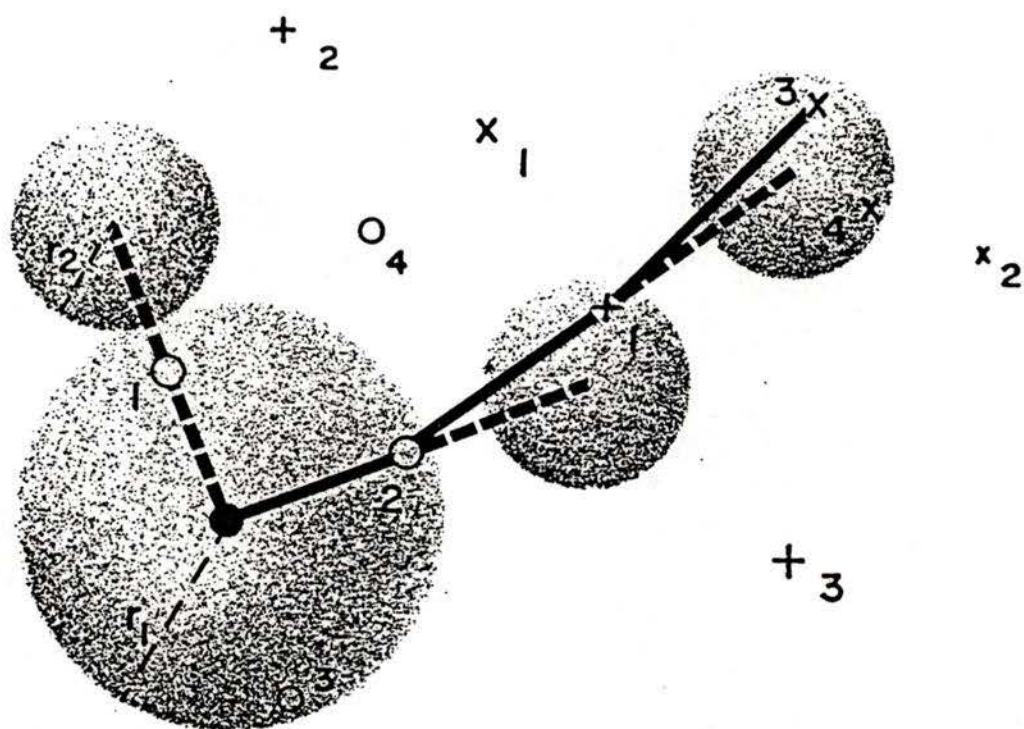


Figure 11. Graphical representation of a hypothetical three-step trajectory tracing process. Symbols identify the frame to which a given tracer location belongs: first ( $\bullet$ ), second ( $\circ$ ), third (+) or fourth ( $x$ ). Numbers identify locations within a frame, and are assigned arbitrarily.

considered. This time a tracer position in the third frame, number 1, is found within range, and the two-step trajectory leading to it is therefore accepted. In the next iteration, the most recently constructed step is used to predict the position in the fourth frame. Of the tracer positions in this frame, denoted by  $x$ , numbers 3 and 4 are within the search range. The one nearest to the predicted location, number 3, is selected as successor. The three-step trajectory obtained is shown as a solid line.

Tracking was attempted on all tracer positions in one frame before a new frame was considered. Trajectories were therefore built in a parallel fashion, as opposed to following a single trajectory from beginning to end before considering another. Since positions that were assigned to one trajectory became irrevocably unavailable to others, the order in which trajectories were processed determined in some cases which path was allowed to continue. It was found preferable for the procedure to give priority to well established trajectories, that is, trajectories whose life span in number of frames was the longest. The search for successors was therefore performed in order of tracer seniority. New tracers were processed in whatever order they were given by the matching algorithm, but only after an attempt had been made to extend the trajectories of all known tracers in their proper turn. This hierarchy protocol insured that in cases in which two tracers both found the best successor in the same position, the longer lived of the two had priority. If alternative successors existed nearby, the other tracer would then choose the best among them to continue its path.

To implement the search procedure, data for three frames must be available to the program at all times. In accordance with Chang and Tatterson (1983), these frames were named F-1, F and F+1. At the beginning of a run, all particles in F-1 were unknown and therefore underwent the two-stage tracking to find their path through F and F+1. The old F-1 was then discarded, F became F-1, F+1 became F and the next frame was read into F+1. On all iterations that followed, tracers in F-1 that were assigned as part of a trajectory already knew their successor in F from the previous iteration, so their new positions could be predicted and successors sought in F+1. Tracers in F-1 that were not part of known trajectories were processed next, and they underwent two-stage tracking. The frames were again shifted back one position and the process continued until F+1 was the last frame in the set. By using a system of pointers to relate a given tracer position to its successors in the two following frames it was possible to streamline processing and make efficient use of memory space. When the data for the F frame was transferred to the F-1 frame after each iteration, it was re-organized so that all tracer positions that formed part of continuing trajectories were placed at the top of the arrays in order of decreasing life span, followed by positions of newly found tracers. Similarly, the data for the F+1 frame was moved to the F frame so that the top elements contained the successors to the corresponding points in the F-1 frame, followed by positions still unassigned. Tracers that had been lost or could not be tracked at all were removed from the arrays during the transfer. The hierarchical order previously de-

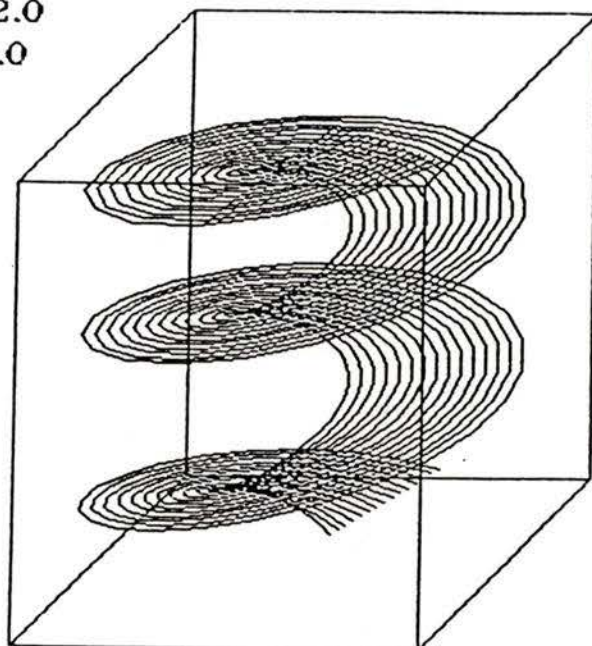
scribed was achieved by simple top-down processing of the arrays, and the number of storage locations required was determined only by the maximum number of tracers visible in one frame during the run. Since information about previous locations of tracers was destroyed as new frames were read in, tracer co-ordinates were plotted on a graphics terminal and/or output to a file as soon as they were identified as part of a given trajectory. The trajectory plot could be generated either as an orthographic projection or as two stereoscopic pairs, representing views from two orthogonal directions. The latter form allowed viewing of the trajectories in apparent tridimensionality. Each co-ordinate triplet in the output file was accompanied by the number of the frame in which it appeared and a serial number identifying the trajectory to which it belonged.

Figures 12 and 13 show an example of graphic output from the tracking program, in orthographic and stereoscopic form respectively. The positional data being processed here was mathematically generated, as part of a preliminary testing phase in which the tracking program's capabilities were evaluated 'on paper' at various levels of tracer concentration and trajectory complexity. In this case, fifteen 'particles' were made to move along concentric helices of constant  $z$  velocity and monotonically increasing angular velocity, common to all. As it may be seen from the tracking statistics in figure 12 and from the plotted paths, every tracer was followed flawlessly. The velocity information obtained from these test trajectories will be used later in the thesis as sample data for successive processing steps.

HELIX001 to 060

range\_new = 12.0

range\_old = 6.0



points: 900

untracked: 0

number of trajectories: 15

longest particle life: 60 frames

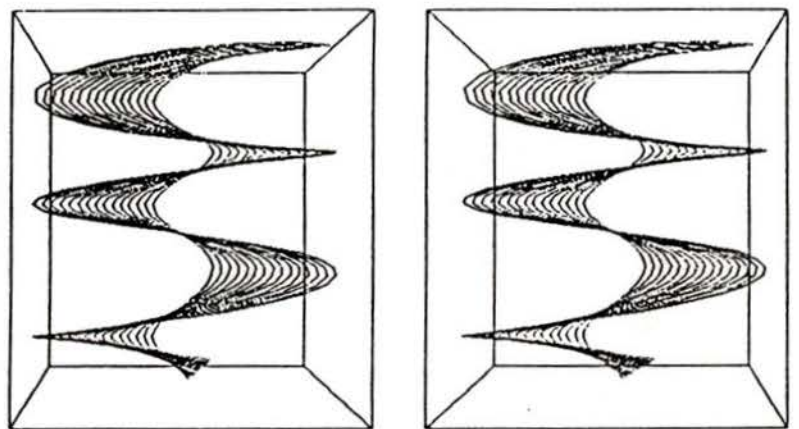
average trajectory life: 60.0 frames

Figure 12. Sample orthographic output of the tracking program, with mathematically generated data. The points being followed lie on helices advancing in the z direction. Front face of outlined volume is contained in the x-z plane.

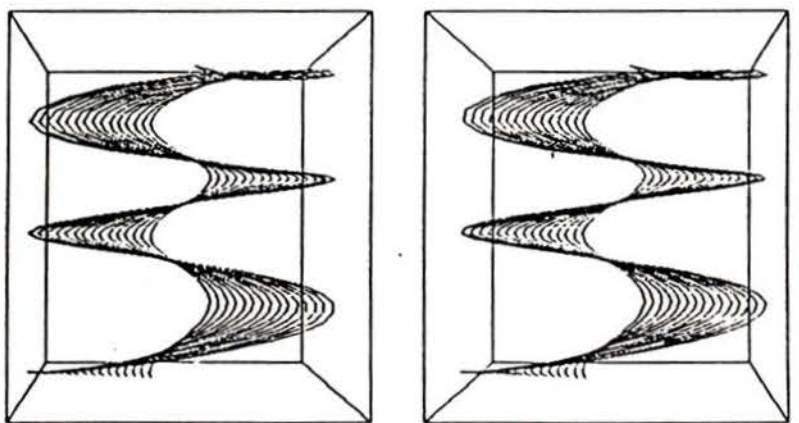
HELIX001 to 060

range\_new = 12.0

range\_old = 6.0



x-z view



y-z view

Figure 13. Sample stereoscopic output of the tracking program. Top pair and bottom pair represent views through the x-z and y-z planes respectively. Positional data is the same as in figure 12.

The two-stage tracking method could also have been applied to known trajectories, instead of routinely taking the tracer nearest to the predicted position as a successor. It would then have been possible to consider alternative choices within the small search sphere if the first selection did not lead to a further successor in the next frame. This scheme, however, does not serve as useful a purpose as it does for the case of new tracers. Provided the filming rate is sufficiently high, the actual position of a successor is closely approximated by the linear extrapolation scheme. Thanks to the greater resolution between tracer positions obtained by following paths in three dimensions, the tracer location that is nearest to a predicted position is almost certainly the correct continuation of a trajectory, unless a tracer actually disappears from view. If the concentration of tracers is so high that the previous condition is often violated, then also the more sophisticated tracking method stands a high chance of constructing incorrect trajectories. Especially in consideration of the substantial increase in processing time that would be involved, weighed against an occasional benefit in terms of accuracy, the scheme outlined above did not appear warranted.

It was found that the size of the search sphere built around predicted positions was crucial for the success of tracking. The radius should be just large enough to allow for velocity changes from frame to frame, and this depends on the type of flow under study and the filming rate. Usually it was best to start with a small value and progressively increase it if the trajectories appear broken into segments.

Ideally, search ranges for different predicted positions should never overlap, so that there is no possibility of one trajectory being extended to a position that belongs to another. However, even if this is not the case the probability of a switch between adjacent trajectories is limited because the velocity field contains no discontinuities. If two paths become so narrowly spaced that there is extensive overlap of search ranges, the velocity vectors must be very nearly parallel in that section, thus reducing the chances of a cross-over. Note that this would not be true if trajectories were followed in a single view, since apparently adjacent paths could in fact be located in entirely different areas of the flow field.

The search range used for new particles, on the other hand, was found not to be overly critical, since it simply represents a stopping criterion for the search if a trajectory cannot be started. It should be larger than the maximum expected displacement from frame to frame, but not exceedingly large to avoid a needlessly long search time and the risk of starting stray 'trajectories' on roughly aligned but widely spaced points.

#### 4.3 Processing of the positional data

At the end of the trajectory tracing stage, the spatial co-ordinates of tracers were available in a sequential-access file. Associated with each set of co-ordinates were the frame number and tracer identification. This information allowed complete reconstruction of the time

history of individual tracers during an experimental run, giving a Lagrangian description of the flow. Depending on the application, further processing might be required to describe the flow field in Eulerian form.

Two approaches to calculating velocity from the positional data were investigated. The simpler method was to consider displacement over individual framing intervals. Assuming that during one framing interval  $(t, t+\Delta t)$  a tracer moved approximately in a straight trajectory with little relative change in velocity, its position and velocity at the mid-point of the interval were estimated as:

$$\vec{r}(t+\Delta t/2) = \frac{\vec{r}(t+\Delta t) + \vec{r}(t)}{2}, \text{ and} \quad (4.3.1)$$

$$\vec{v}(t+\Delta t/2) = \frac{\vec{r}(t+\Delta t) - \vec{r}(t)}{\Delta t}. \quad (4.3.2)$$

The assumptions could be considered justified in most cases if the framing period  $\Delta t$  was sufficiently small. The use of single steps had the advantage of giving the best response to changes in velocity, at the risk of maximizing the error in velocity arising from inaccuracies in tracer location.

The second, more elaborate method was to fit least-squares polynomials in  $t$ , one for each co-ordinate, to several consecutive tracer positions and use the time derivatives at the midpoints as velocity components. When a new point was read in, the 'window' for the fit was advanced by one step along the trajectory. The overlap of the fitted sections ensured a certain degree of continuity. The general-purpose

scheme adopted for the present work used four points and quadratic polynomials, but other combinations may be advantageous for specific types of flow. For very smooth trajectories it would be possible to fit polynomials of reasonably low degree through longer intervals and obtain derivatives at several locations along the fitted curve.

In some cases, knowledge of the position and velocity of individual tracers as they move through the field may be useful in its own right.

In the domain of artificial heart valve testing, for example, it is often desirable to locate pathlines that lead to areas of flow stagnation, which is considered dangerous because of its potential for thrombus formation. The ability to record the trajectories of fluid elements makes the particle-tracking technique more versatile than point-oriented flow measurement methods such as laser doppler anemometry, with the added advantage that data for various areas of the flow field is gathered simultaneously. A drawback is the aleatory nature of the spatial distribution of data points, since direct information is only available for those positions where one or more tracers happen to travel during the experiment.

For many applications, on the other hand, it is desirable to obtain Eulerian velocity information about the entire flow field under study. In the present work, this was done by pooling the velocity data obtained from various tracers and interpolating at points where tracers were not found. The data which could be pooled depended on the type of flow under investigation. If the flow was steady, data from all frames in a sequence could be merged to increase the effective sampling

density. If the flow was non-steady but time-periodic, such as may be encountered in physiological situations, data from frames taken during the same phase of the cycle in successive periods could be pooled to obtain a 'snapshot' of the velocity field in that phase. In the case of unsteady and non-periodic flows only statistical data about the mean flow field could be collected by pooling of successive frames. The concentration of tracers in a single frame would seldom be sufficient to allow meaningful interpolation of the instantaneous velocity field.

The pooled velocity data were divided into components, giving three sets of values at specific locations in space. Each set described a hypersurface  $f(x,y,z)$  by points, where  $f$  was  $v_x$ ,  $v_y$  or  $v_z$ . The hypersurfaces were individually evaluated on a regular three-dimensional grid. The distance between grid points determined the spatial accuracy to which the flow velocity field was described, and hence the size of the flow features that could be resolved.

The algorithm that built each hypersurface through the data points was obtained by extending a procedure developed by the Marine Environmental Data Service to interpolate data of the form  $z(x,y)$  on a regular two-dimensional grid (Taylor et al., 1971; Taylor, 1976). The latter reference gives a functional description of the original method, in which the surface was considered as a mesh of rigid rods connected by joints elastically bendable in the  $z$  direction. The smoothness of interpolation was determined by specifying the elasticity constant. Stiffer joints yielded a smoother surface but increased the risk of overshoots in areas devoid of data points. The approach for a three-

dimensional grid is equivalent, although it can no longer be understood in terms of an intuitive model. The algorithm was modified in the present work by rewriting each expression in the original code as a function of three variables and altering the logic flow to include the processing of an extra dimension in the grid array. The procedure was tested on various data sets generated from continuous functions of three variables, and was found to yield well-behaved hypersurfaces even at low concentrations of data points. The large number of computations needed to compute the hypersurfaces placed a practical bound on the number of grid elements. For a 20x20x20 grid, a typical run (for all three components) took about one CPU hour on a VAX 11/750. For a 40x40x12 grid with the same data, truncating each interpolation after 150 iterations, almost three hours of CPU time were required. It was found that beyond 100 iterations convergence was in most cases very slow, though steady. Even if full convergence to the required tolerance was not achieved within the iteration limit, the shape of the hypersurfaces was always sufficiently well defined to give a satisfactory interpolation. This fact had already been observed by Taylor (1976) for the two-dimensional case.

Once the velocity components had been interpolated on a regular grid, the velocity field could be presented by a variety of means. If the velocity magnitude alone was of interest, the task of displaying the scalar field was handled by visualizing its value on individual cross sections of the grid, usually taken perpendicular to the z axis. Scalar velocity could then be displayed as a color-coded map. A

program was developed that generated high-resolution maps from the gridded data and displayed several cross sections at once or any selected cross section enlarged to full screen size on the monitor of the image processor. Linear interpolation in the x and y directions was used to generate a smooth looking map from the relatively coarse grid obtained from the hypersurface computations. Figures 14 and 15 are sample velocity map outputs, obtained from the mathematically generated helical trajectories described earlier. In figure 14 the cross section labelled 1 has the lowest z value, the one labelled 10 the highest. The increase in tracer velocity with radius and with z position is clearly represented by the color changes. These and all following velocity maps are shown in two color schemes, one resolving 255 different hues and the other only 20. Either scheme was found to have certain advantages over the other for specific purposes: the 255-color display was smoother and gave a better overall idea of the field trends, whereas the 20-color output exhibited a 'contouring' effect that was useful in determining isotachs. The mapping program could switch instantly from one mode to the other by loading different translation tables in the image processor.

The display of the entire vector velocity field posed a more difficult problem. Flow fields that did not contain small-scale features were satisfactorily portrayed by plotting the velocity vectors at every point of a coarse grid, either as an orthographic projection or as stereoscopic pairs. Figures 16 and 17 show these types of output for the velocity data from the helical trajectories.

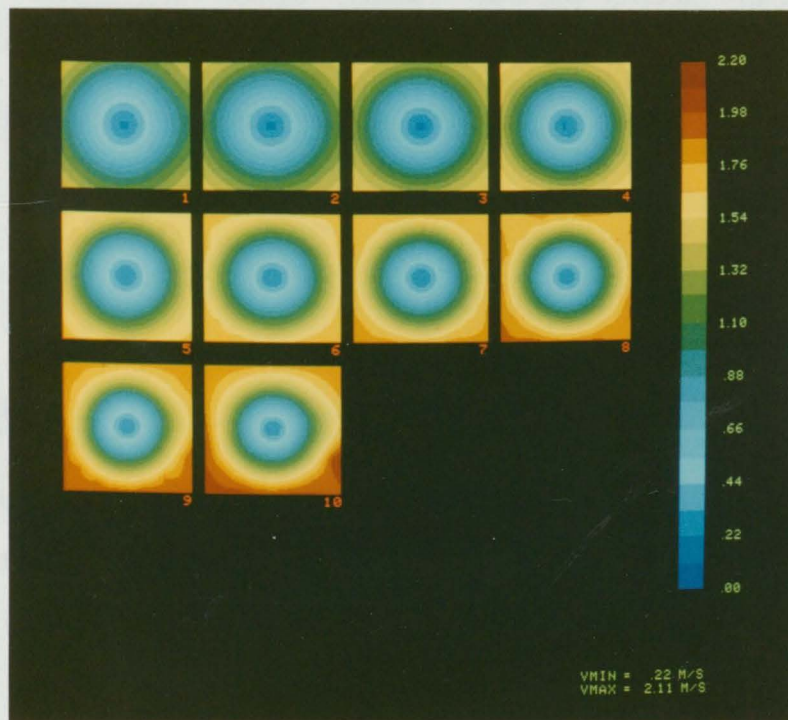
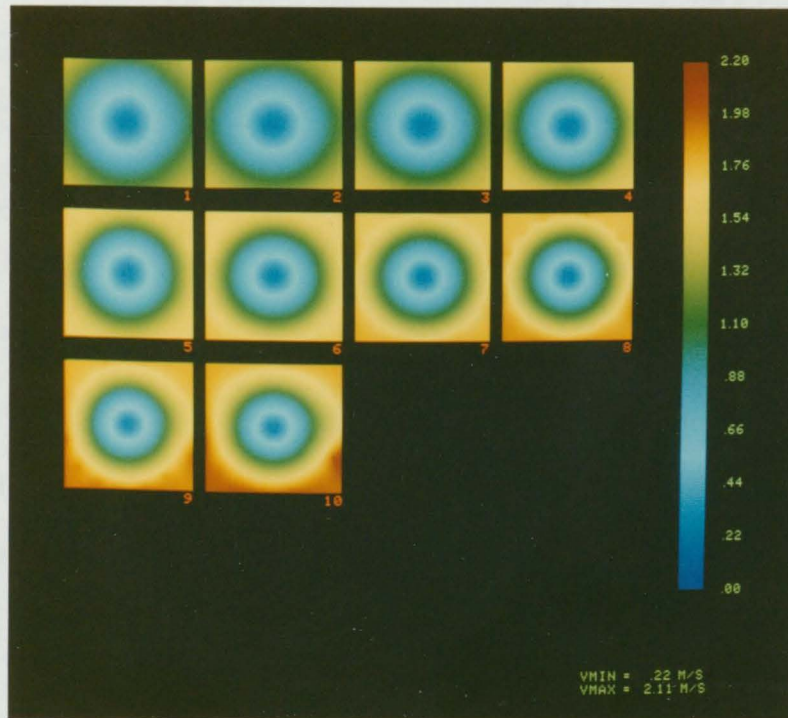


Figure 14. Scalar velocity maps from the helical trajectories of figure 12. Sections are parallel to the x-y plane. Interpolation over a  $20 \times 20 \times 10$  grid. Top image: 255 colors; bottom image: 20 colors.

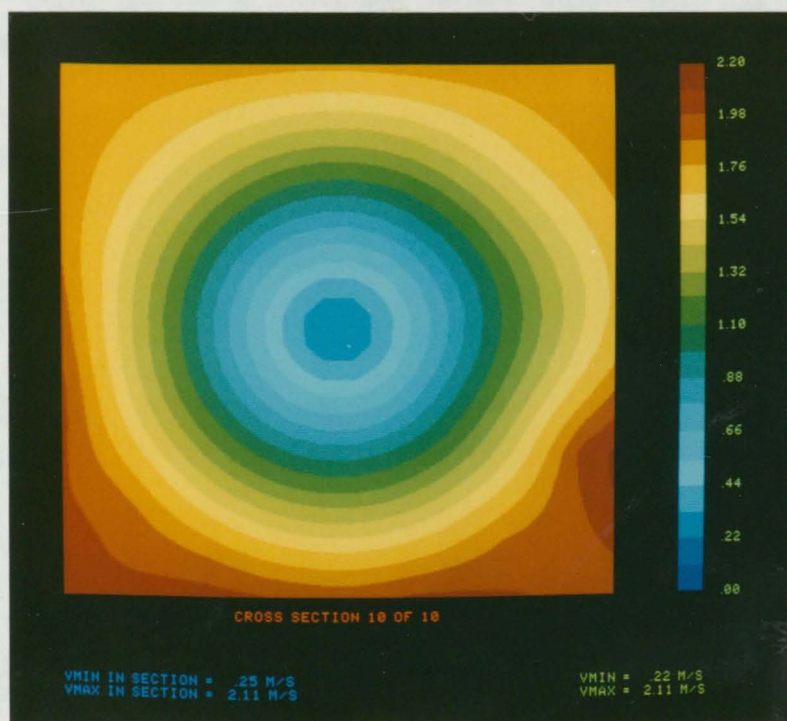
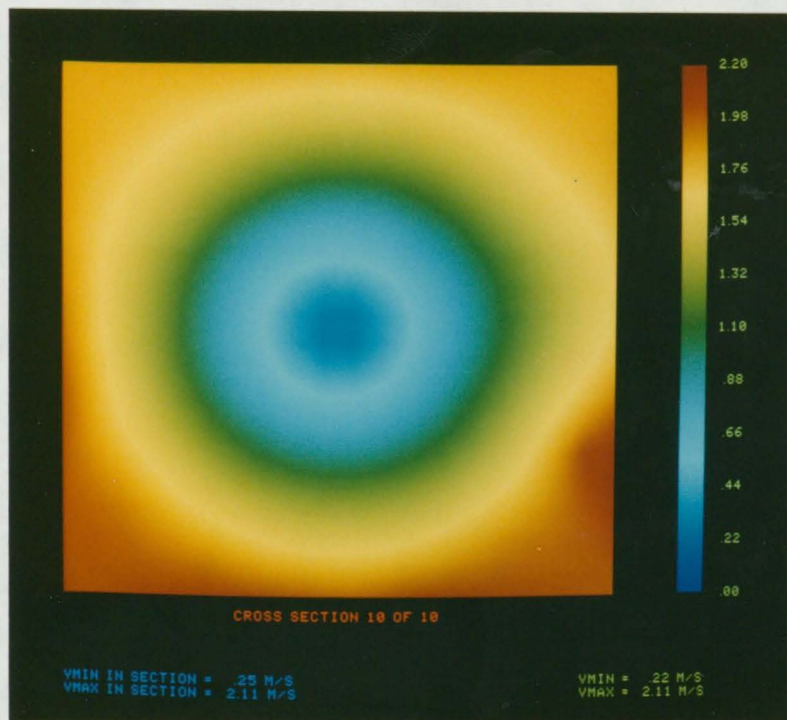


Figure 15. Full-screen display of a velocity map from figure 14.

HELIX001 to 060

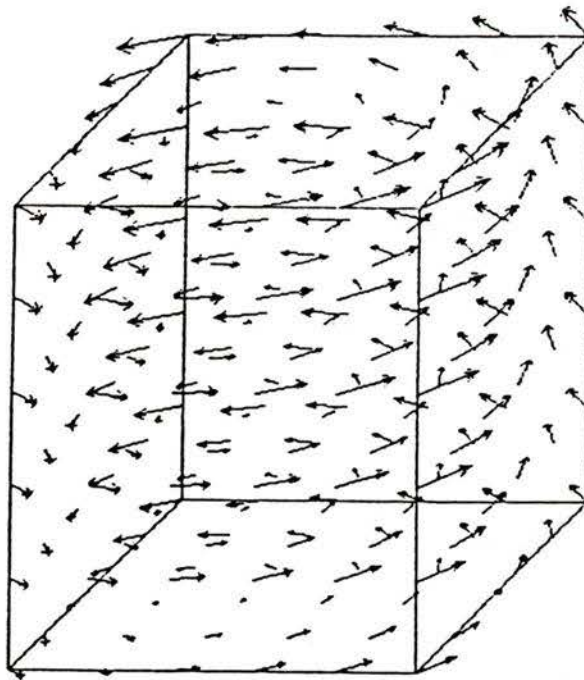
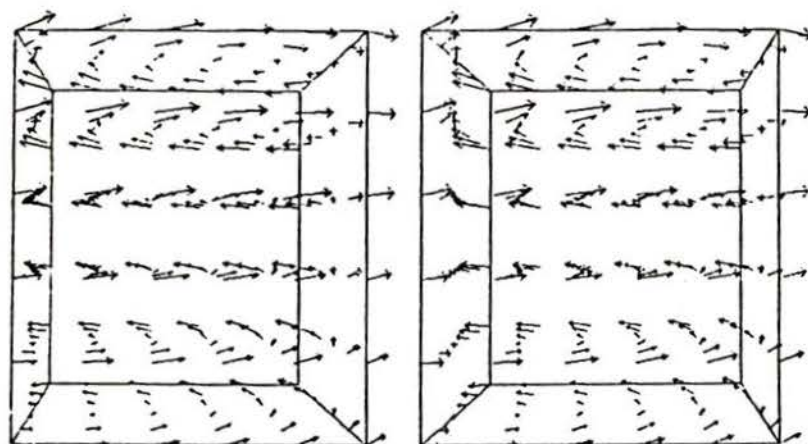
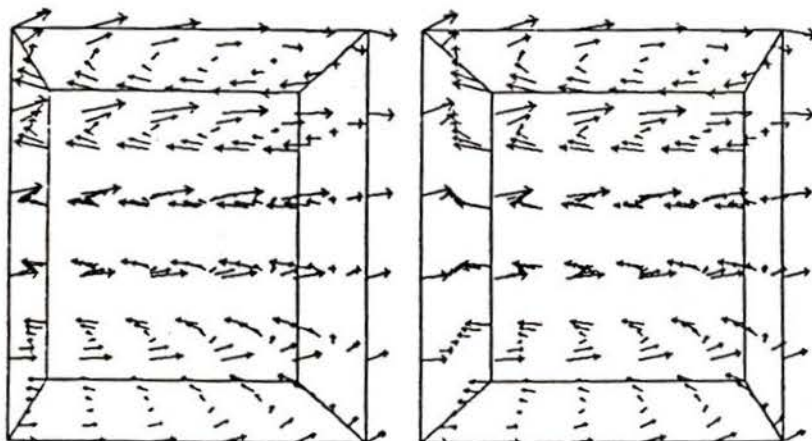


Figure 16. Orthographic output of vectorial velocity field from the helical trajectories of figure 12. Interpolation over a 6x6x6 grid.

## HELIX001 to 060



x-z view



y-z view

Figure 17. Stereoscopic output of vectorial velocity field from the helical trajectories of figure 12. Interpolation over a 6x6x6 grid.

The orthographic display had the apparent advantage of requiring no special devices for observation, but visual ambiguity was unavoidable as to the location and exact orientation of various vectors. Stereoscopic images removed the ambiguity and gave an excellent feel for the spatial characteristics of the flow field, but could be cluttered if a high density of vectors was used. As the grid spacing was reduced to increase the resolution, the overlapping of vectors made the output unreadable.

The problem of cluttering might be alleviated by presenting the output as a computer-generated multiplex hologram, which would allow the viewer to choose the most appropriate direction for observation. Use of this method to display three-dimensional flow visualization results has been discussed by Hesselink et al. (1983). The technique involves generating a large number of perspective or orthographic views of the field, each seen from a slightly different angle, and from each view create a thin holographic strip by conventional optical means. The many strips, recorded side by side on large-format sheet film which is then curved in a circle, create a composite hologram that allows stereoscopic observation of the field from all azimuthal angles, since each eye sees a different perspective of the image through a separate holographic strip. A combined time-space display of non-steady flow fields can be obtained if each view represents a slightly later moment in time than the previous one. This type of time sequential display has some disadvantages, mainly the fact that the flow at any given time can only be observed from one angle of view and that the two eyes see

images of the field corresponding to different times. Correction methods for the last problem, known as 'time smear', have been presented by Dutta et al. (1983). Because of the substantial amount of experimentation involved in developing a working system, production of multiplex holograms was not undertaken as part of the present study.

## CHAPTER 5

### TESTING AND EVALUATION

#### 5.1 Test flow channel

To produce controlled flows of various kinds on which to test the automatic particle tracking procedure, the simple flow channel shown in figure 18 was built. A vertical design was chosen to simplify construction and optimize optical accessibility. The overall height of the structure was 570 mm, and the column had a square internal cross section with sides of 70 mm. The test section was 250 mm high. All modular components were fabricated out of clear plexiglas and secured together by flanges, with interposed 'O' rings to seal the joints. The fluid flowed in a closed circuit, powered by a 125 W submersible pump with rated capacity of about 70 l/min at a pumping height of 1.5 m. One-inch PVC tubing was used for inflow and outflow connections to the channel. The pump drew from a free-surface return reservoir and injected the fluid into the base of the device. The base chamber gave stability to the free-standing structure and allowed the jet from the input tube to expand into a random vortical motion. Ceramic pre-filter material (FLUVAL), held together by a plastic net, partially filled the base and helped to break up the flow. The fluid emerged into the bottom of the column through a 7 wires/cm fiberglass screen and passed through a section containing closely packed flow straighteners, each 5 mm in diameter and 50 mm long. By direct observation of tracers in the

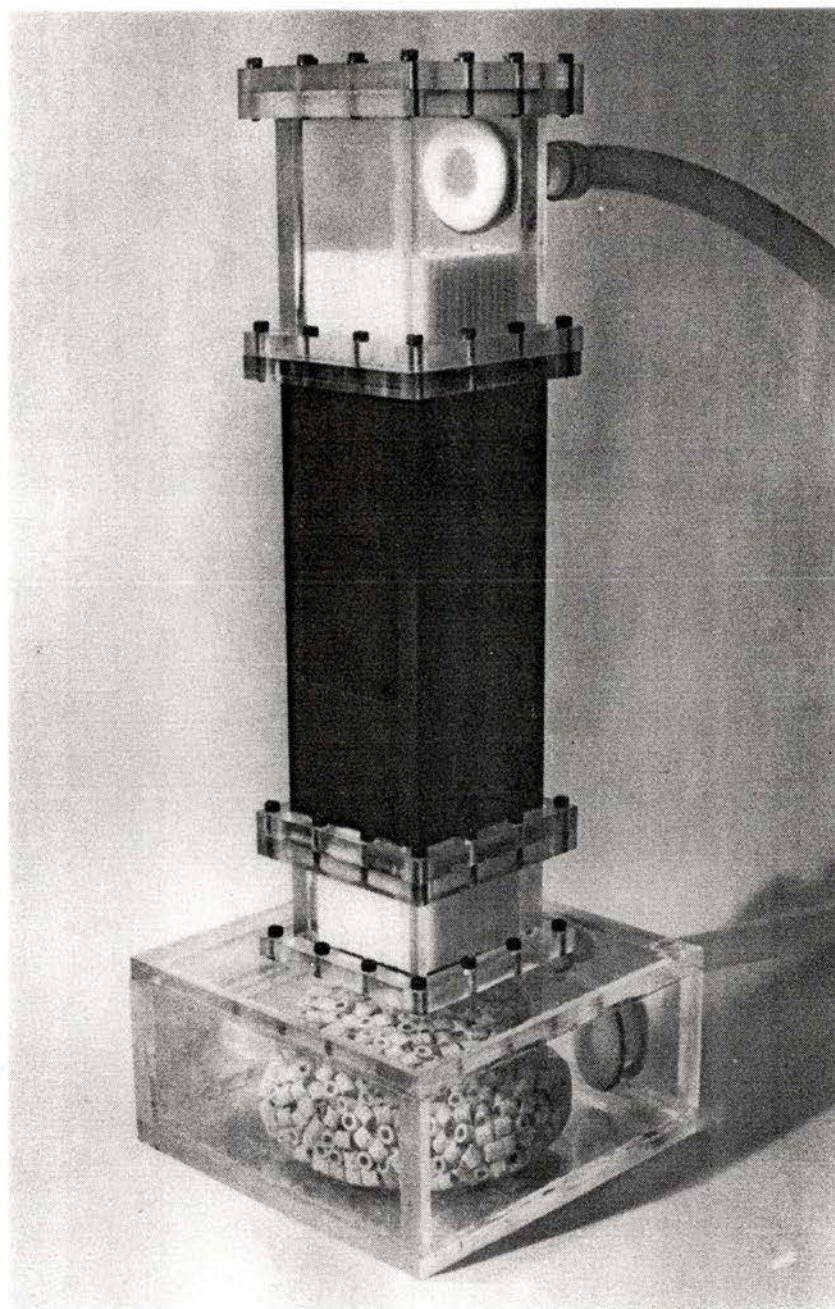


Figure 18. Test flow channel.

fluid it was verified that the flow entering the test section had a reasonably flat velocity profile and limited small-scale turbulence. On the basis of the pump rating, the nominal flow velocity that could be obtained in the unrestricted test section of the column was estimated to be of the order of 0.24 m/s. The test section was painted flat black externally with the exception of two centered windows on adjacent sides, 70 mm wide by 80 mm high. The observable volume therefore covered the whole cross section of the channel for a length of 80 mm, with sufficient room upstream or downstream to install models. White dots were placed at the corners of the windows to serve as fiducial marks. The sides opposite the windows were painted flat black internally to give maximum contrast to the tracers. Above the test section, a set of flow straighteners identical to the bottom ones prevented the sideways flow through the outlet from disturbing the fluid motion in the working volume. The fluid returning to the reservoir was directed inside a small overflow tank that broke up the high-speed flow, to avoid the possibility of air bubbles being churned near the pump intake.

## 5.2 Testing runs

Tests of the entire analysis procedure on actual flows were carried out using the water channel and recording equipment previously described. The working fluid was tap water containing a small amount of surface tension reducing agent (Kodak Photo-Flo) which helped to dislodge small air bubbles adhering to the sides of the column. Amberlite

IRA-904 (Rohm and Haas Company, Philadelphia) resin beads, sieve screened to obtain a uniform size of about 300 microns, were used as flow tracers. The use of this material was suggested by Wieting (1969) in his doctoral thesis.

The particles were slightly denser than the working fluid, and therefore they may not have followed the flow with great accuracy under all conditions. It is generally accepted that errors due to density mismatch are minimized if the main flow direction is vertical and the rate of rise or fall of particles in the fluid is small compared to the flow velocity. Charwat (1977) showed that in a vorticose flow, particles having density different than the working fluid will consistently exhibit motion relative to the flow. As the size of tracers is reduced, problems due to density mismatch become less pronounced (Roberson, 1955). On the other hand, it becomes increasingly difficult to obtain sufficient light scattering from the tracers as their size decreases, so that a compromise must often be achieved. The question of how accurately the particles followed the flow was not of particular relevance here, since all that was asked of the experimental equipment was to generate sufficiently realistic particle paths on which to evaluate the procedure.

Some of the experiments were recorded on black and white negative film (Kodak RAR 2479), which allowed immediate processing. Better resolution and contrast were obtained by using color reversal film (Kodak Ektachrome 7250). The scene analysis program could indifferently handle positive or negative images.

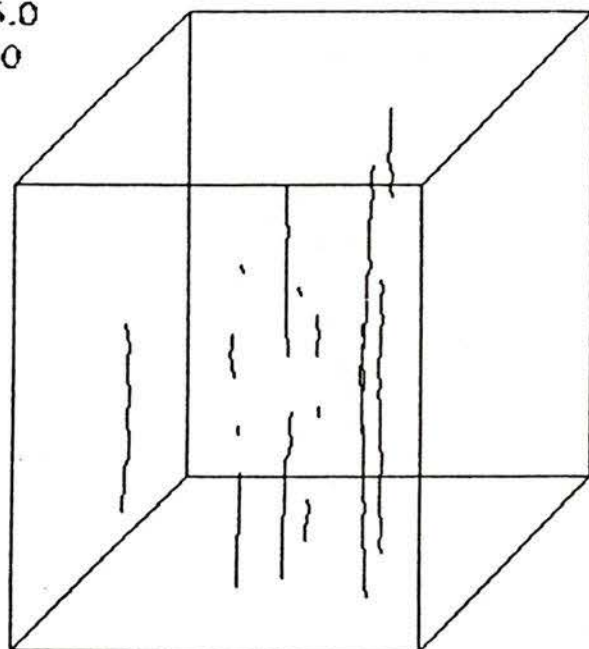
In these evaluation runs, the concentration of particles in the fluid was kept low, giving at most about 10 tracers visible at once in the test volume. This simplified the task of checking the accuracy of the tracking procedure by direct observation of the tracer motion in the projected films. More demanding situations were then artificially created from the original data by mirroring the three-dimensional particle field in each frame about various planes parallel to the main flow direction, thus increasing the concentration of virtual tracers dispersed through the visible volume.

The motion of tracers in the free column flow was analyzed in one of the tests, to verify the quality of the reconstructed velocity field in a controlled situation. The camera was located at an effective distance from the windows, including the path length inside the mirror box, of 1500 mm. The film was exposed at 200 pictures per second. Upon inspection of the processed film, it was determined that the framing rate was needlessly high for the average velocity of the tracers. Only alternate frames were therefore considered, thus reducing the effective framing rate to 100 pps. Thirty frames from the sequence were analyzed. On the average, about 8 tracers were matched in the perpendicular views in each frame. The graphic output of the tracking procedure, using search ranges of 5.0 and 3.0 mm for new and known tracers respectively, is shown in figures 19 (orthographic) and 20 (stereoscopic). A total of 230 out of 252 points were identified as part of trajectories, leaving 22 untracked as indicated in figure 19. Eighteen trajectories were followed, the longest extending throughout the 30 frames. The

CLR001 to 030

range\_new = 5.0

range\_old = 3.0



points: 252

untracked: 22

number of trajectories: 18

longest particle life: 30 frames

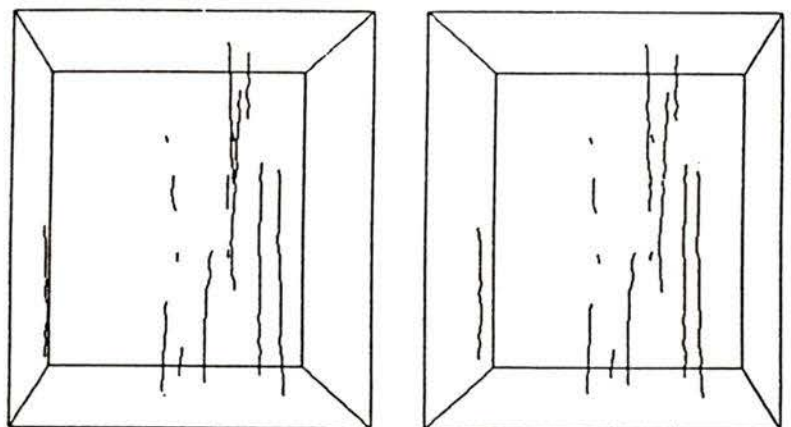
average trajectory life: 12.8 frames

Figure 19. Orthographic output of tracer paths in the unrestricted column. Analysis of 30 frames taken at 0.01 s intervals.

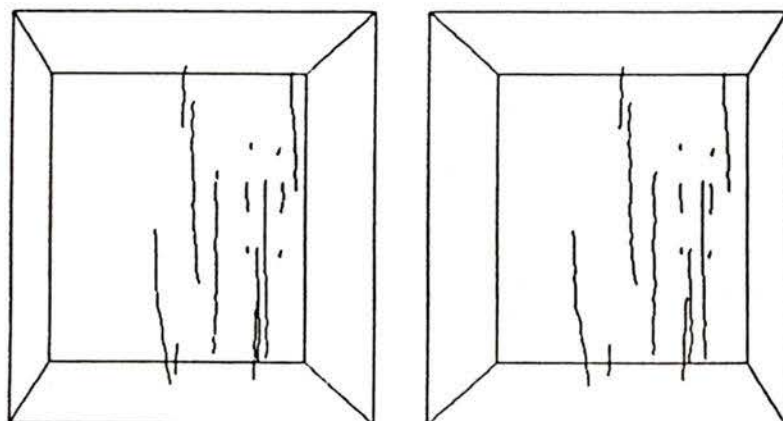
CLR001 to 030

range\_new = 5.0

range\_old = 3.0



x-z view



y-z view

Figure 20. Stereoscopic output of the trajectories of figure 19.

average trajectory survival period was 12.8 frames. By four-point polynomial fitting and differentiation of the trajectories 176 velocity data points were obtained. Interpolation of these points on a regular 6x6x6 grid yielded the vector velocity field shown in figure 21. The near uniformity of vector magnitude and direction throughout the field is consistent with the nature of the flow under study (velocity profiles in the boundary layer are not revealed). Flow speed ranged between 0.16 and 0.20 m/s, with no specific distribution of highs and lows. The mean flow speed conforms within reason to the estimated upper limit of 0.24 m/s based on the pump rated capacity and cross sectional area of the column. Figure 22 shows a set of flow speed maps obtained from a 40x40x10 interpolated grid, and figure 23 shows one such map enlarged to full screen size. The uniformity of the field is clearly shown by the color distribution being limited to a narrow range of the scale. It may be noticed that in this case the hard-limiting effect of the 20 color encoding scheme gives rather undesirable contours.

Another test recording was performed after restricting the open area of the column by a sharp-edged orifice upstream of the visible section. A 0.003" mylar diaphragm with a centered hole 3 cm in diameter was placed in the column about 1 cm above the bottom flow straighteners. The orifice was almost 3 diameters upstream of the lower edge of the visible section, so that the open jet could break up into an unstable flow before it reached the viewfield. Nevertheless, the volume of fluid directly on axis with the orifice moved in a mainly vertical direction

CLR001 to 030

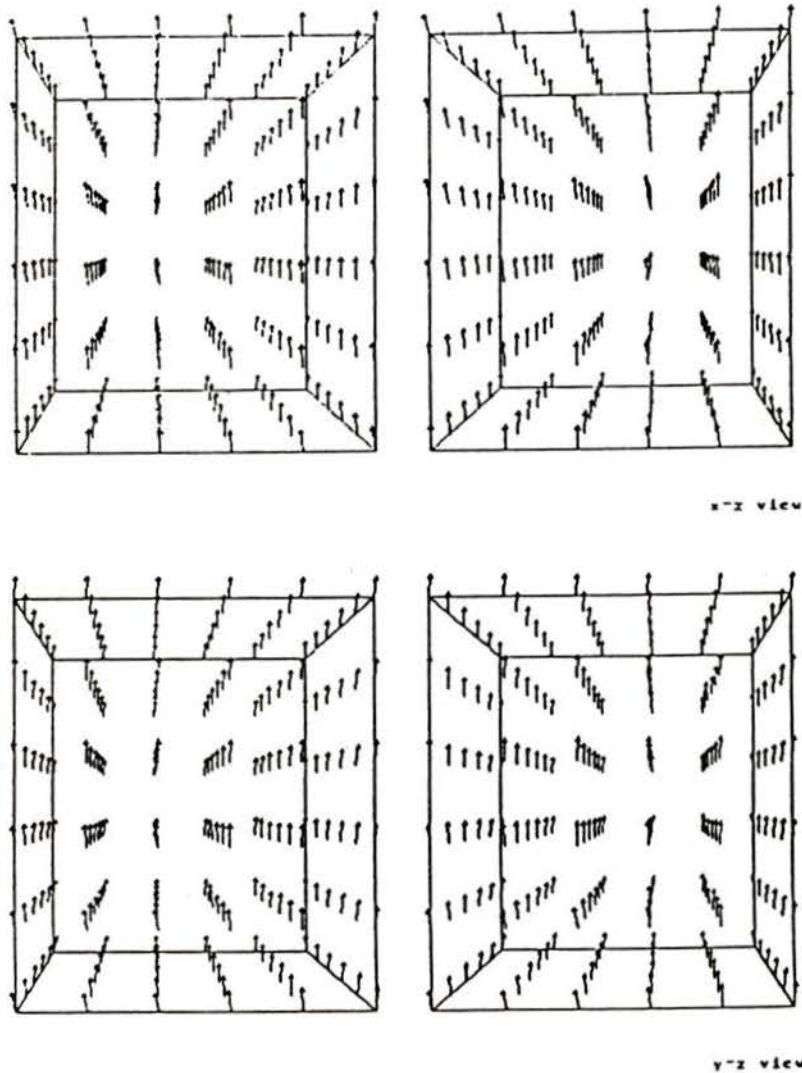


Figure 21. Stereoscopic output of vectorial velocity field for the flow in the unrestricted column. Interpolation over a 6x6 grid.

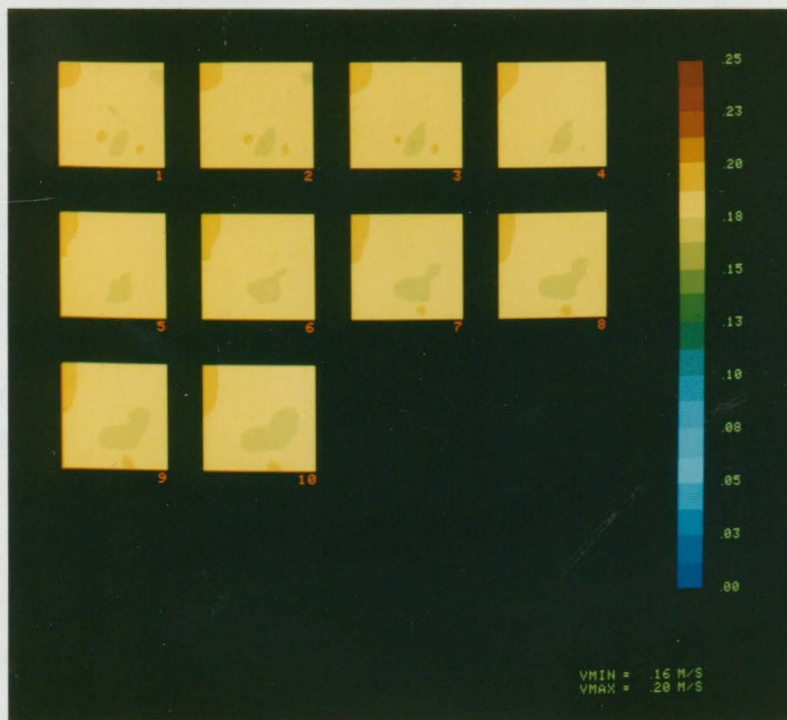
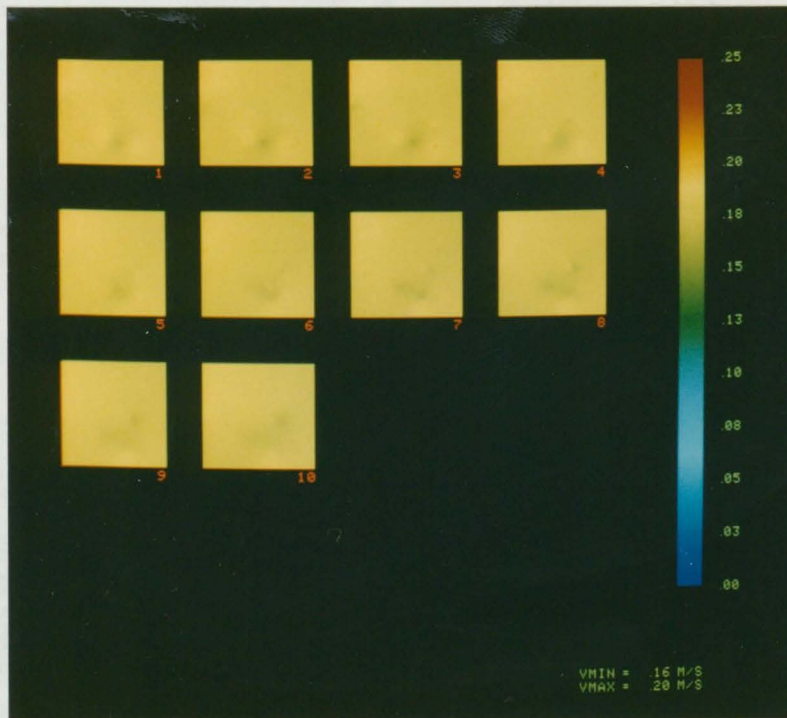


Figure 22. Scalar velocity maps for the flow in the unrestricted column. Interpolation over a 40x40x10 grid.

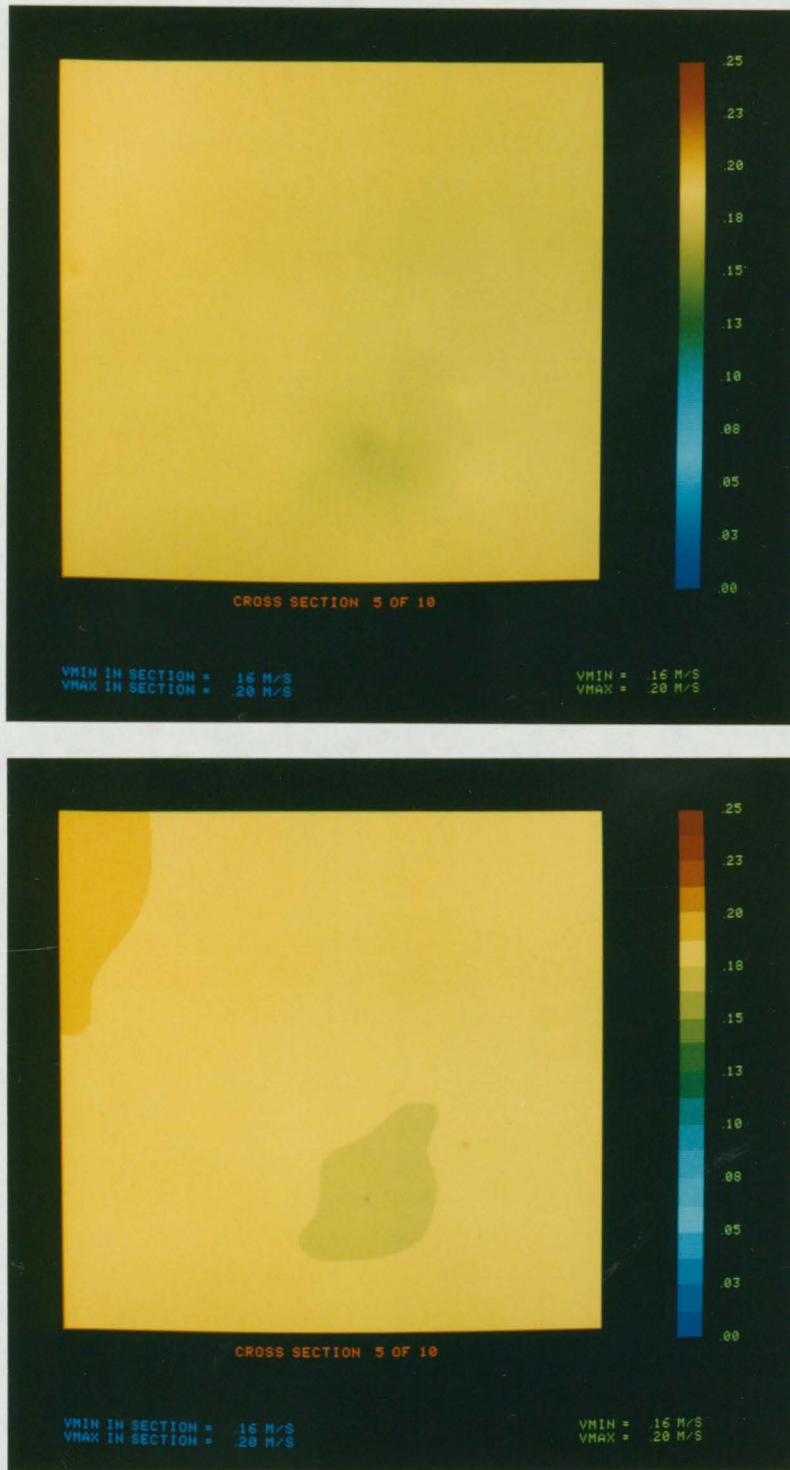


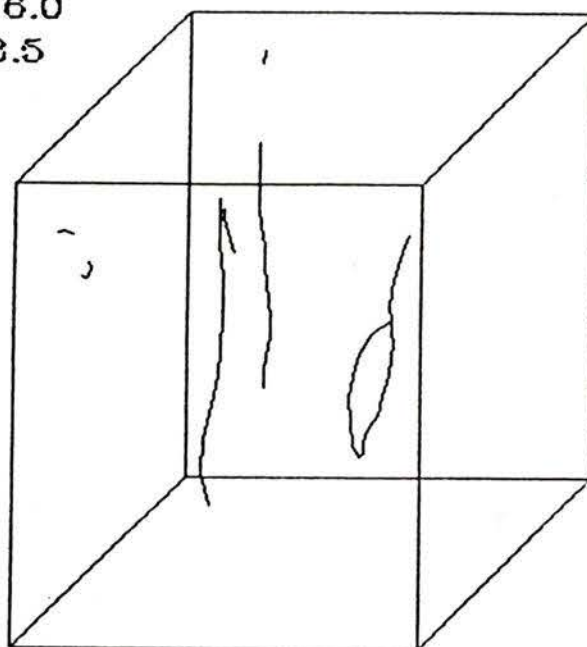
Figure 23. Full-screen display of a typical velocity map for the unrestricted column flow.

at a higher speed than the surrounding fluid throughout the height of the visible section. This was easily noticed by direct observation of tracer motion on film. The flow was filmed at a framing rate of 200 pictures per second, and 30 consecutive frames were analyzed. Only 3 tracers on the average were visible in each frame for this experiment. Automatic tracking was performed with parameters of 6.0 mm and 3.5 mm for new and known particles and yielded the trajectories shown in figure 24 and 25. Of 102 matched points, 94 were assigned to trajectories. Eight trajectories were followed, with an average length of 11.8 frames. A tracer that was visible through all 30 frames was tracked without interruption. As revealed by its hook shaped path, noticeable in the mid-section of the field, that tracer was successfully followed through a complete reversal of direction as it entered the central stream from the turbulent fringe area. To increase tracking difficulty, the original tracer distribution was then mirrored in individual frames about two planes of symmetry of the column, each parallel to one window surface. Automatic tracking was performed on the new data using identical parameters as before. The trajectories, shown in figures 26 and 27, corresponded exactly to the ones for the original data and their mirror images, with the exception that one quadruplet of trajectories did find an extra step. The discrepancy occurred because the reflections of a previously untracked point happened to be within continuation range of a set of mirrored trajectories, an occurrence intrinsically due to the symmetrization process. The 284 velocity points from the symmetrized field were interpolated on a regular 6x6x6 grid,

ORF001 to 030

range\_new = 6.0

range\_old = 3.5



points: 102

untracked: 8

number of trajectories: 8

longest particle life: 30 frames

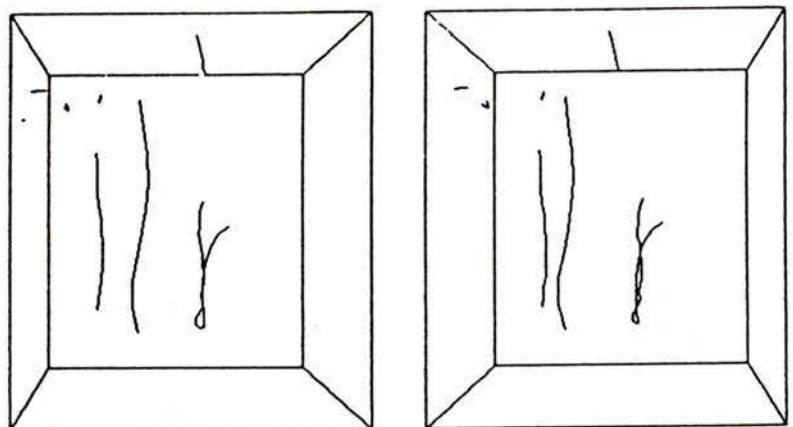
average trajectory life: 11.8 frames

Figure 24. Orthographic output of tracer paths in the column restricted by a sharp-edged orifice. Analysis of 30 frames taken at 0.005 s intervals. The orifice is 3 cm in diameter and is located 8 cm below the bottom of the visible volume outlined in the diagram (for reference, the height of that volume is 8 cm in actual size).

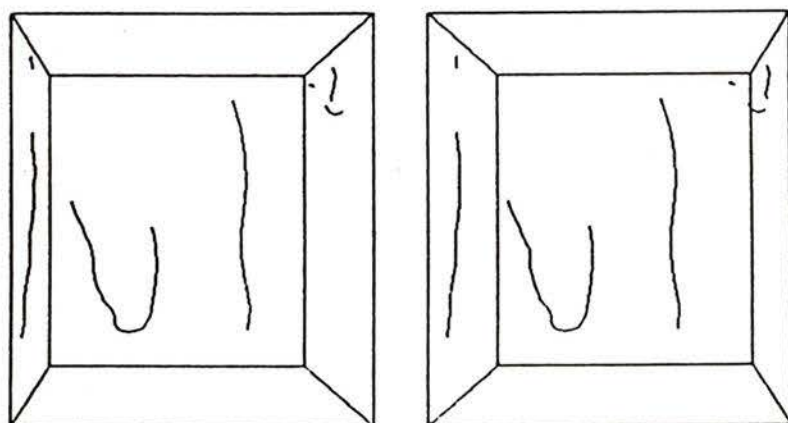
ORF001 to 030

range\_new = 6.0

range\_old = 3.5



x-z view



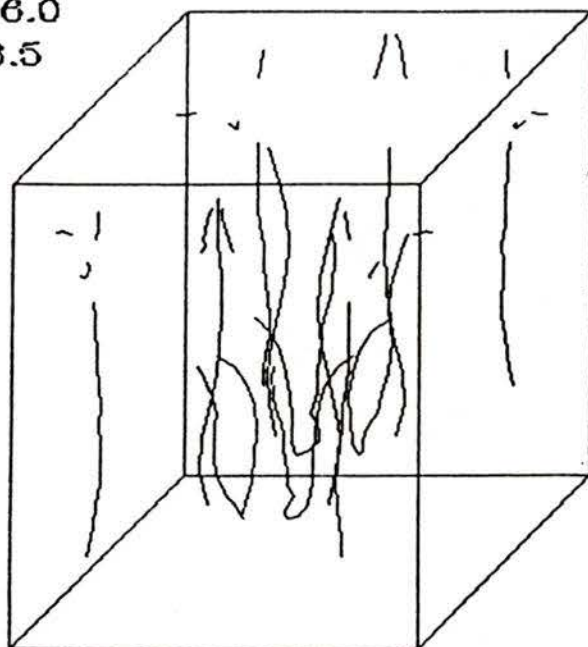
y-z view

Figure 25. Stereoscopic output of the trajectories of figure 24.

ORFREF001 to 030

range\_new = 6.0

range\_old = 3.5



points: 408

untracked: 28

number of trajectories: 32

longest particle life: 30 frames

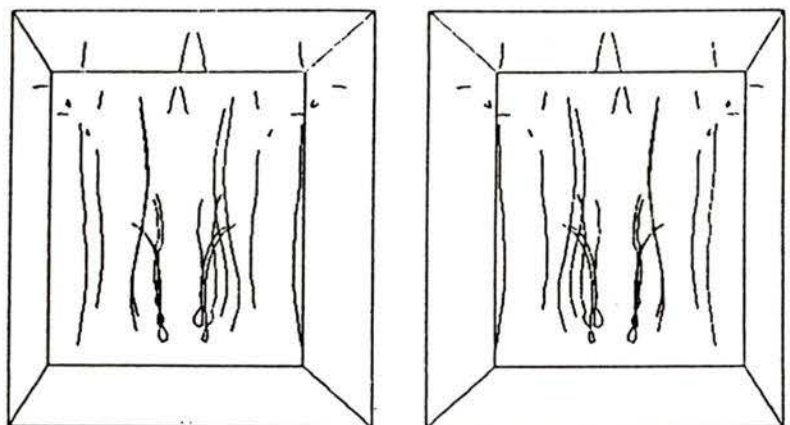
average trajectory life: 11.9 frames

Figure 26. Orthographic output of symmetrized tracer paths in the column restricted by a sharp-edged orifice. Analysis of 30 frames taken at 0.005 s intervals.

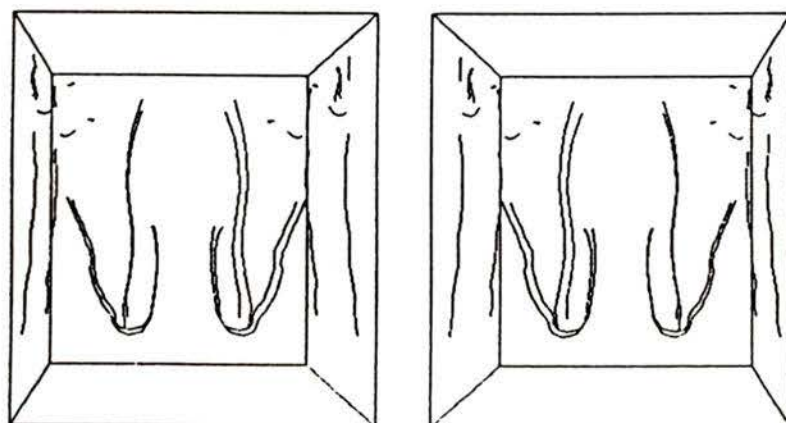
ORFREF001 to 030

range\_new = 6.0

range\_old = 3.5



x-z view



y-z view

Figure 27. Stereoscopic output of the trajectories of figure 26.

yielding the vector velocity field shown in figure 28. Because of the small concentration and uneven distribution of tracers, the value of the velocity field at many locations was not always representative of the actual mean flow velocity there. For instance, the absence of visible tracers in the bottom section of the viewfield caused the central stream of vertically moving fluid to be virtually missed in that area, giving a fairly uniform, low-speed field. Higher up in the test volume, where particles moving in the central flow were detected, the vector field clearly exhibits a central column of fluid moving vertically at higher speed, surrounded by fluid moving in an apparent vortex (downward near the walls, gradually turning upward as it approaches the center). Figure 29 shows a set of flow speed maps obtained from a 25x25x10 interpolated grid. The central higher-speed flow is most obvious in the top sections of the test volume, mainly because little contribution exists there from other trajectories moving in contrasting directions. Figures 30 and 31 show quite plainly the changes in the field from the lower to the upper sections. Although in this example the field characteristics are noticeably influenced by the distribution of the few trajectories, the ability of the interpolation algorithm to build well-behaved hypersurfaces through the data points appears quite satisfactory.

ORFREF001 to 030

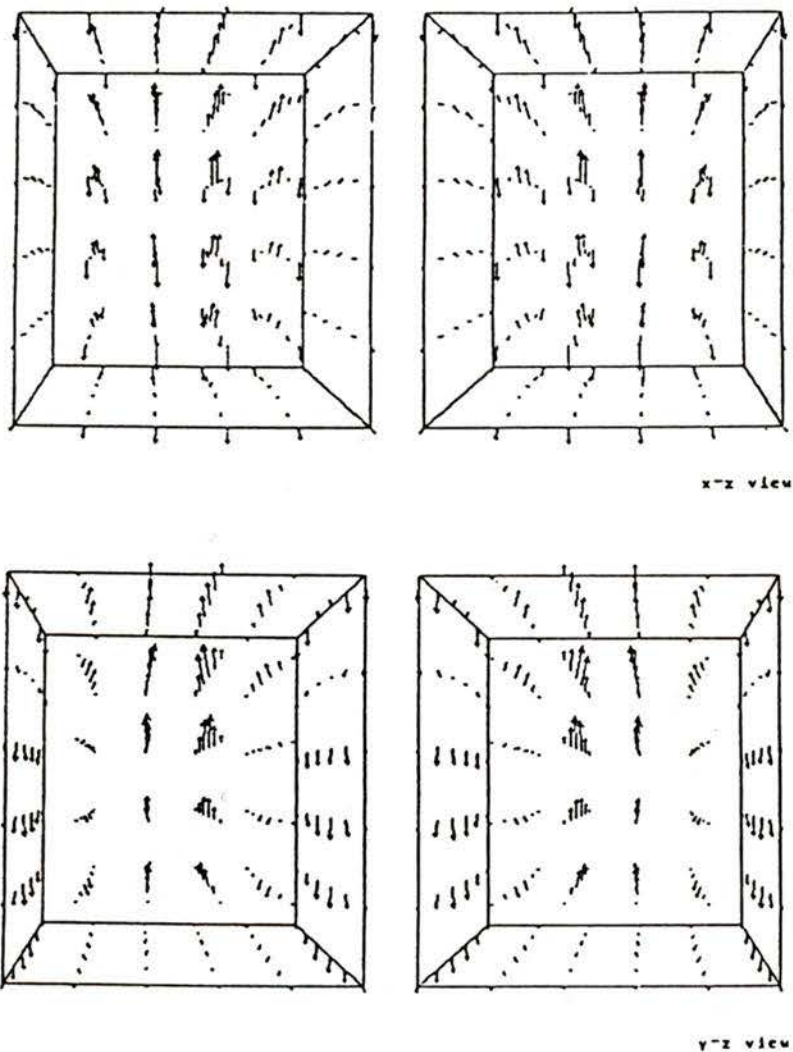


Figure 28. Stereoscopic output of vectorial velocity field for the symmetrized flow in the column restricted by an orifice. Interpolation over a 6x6x6 grid.

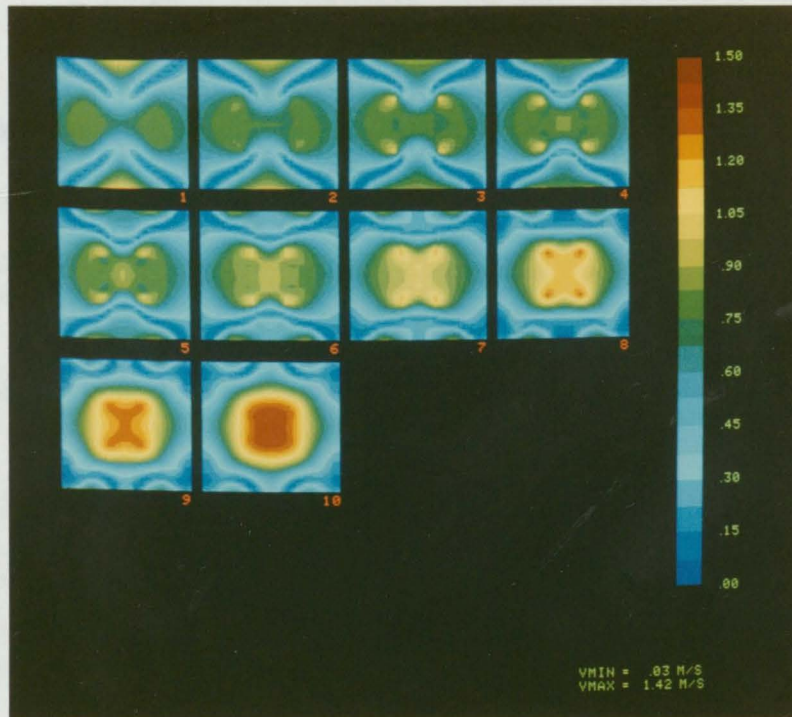
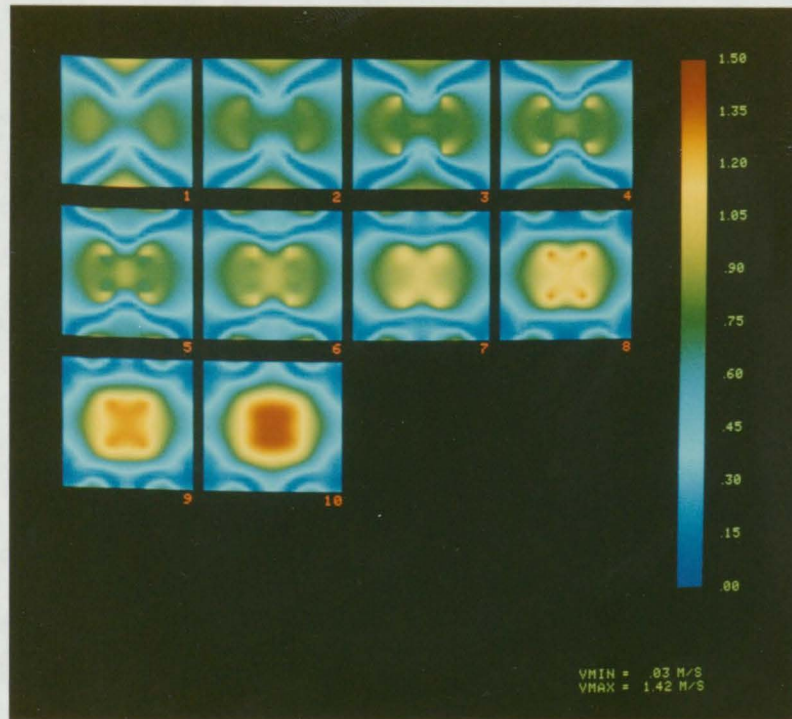


Figure 29. Scalar velocity maps for the symmetrized flow in the column restricted by an orifice. Interpolation over a 25x25x10 grid.

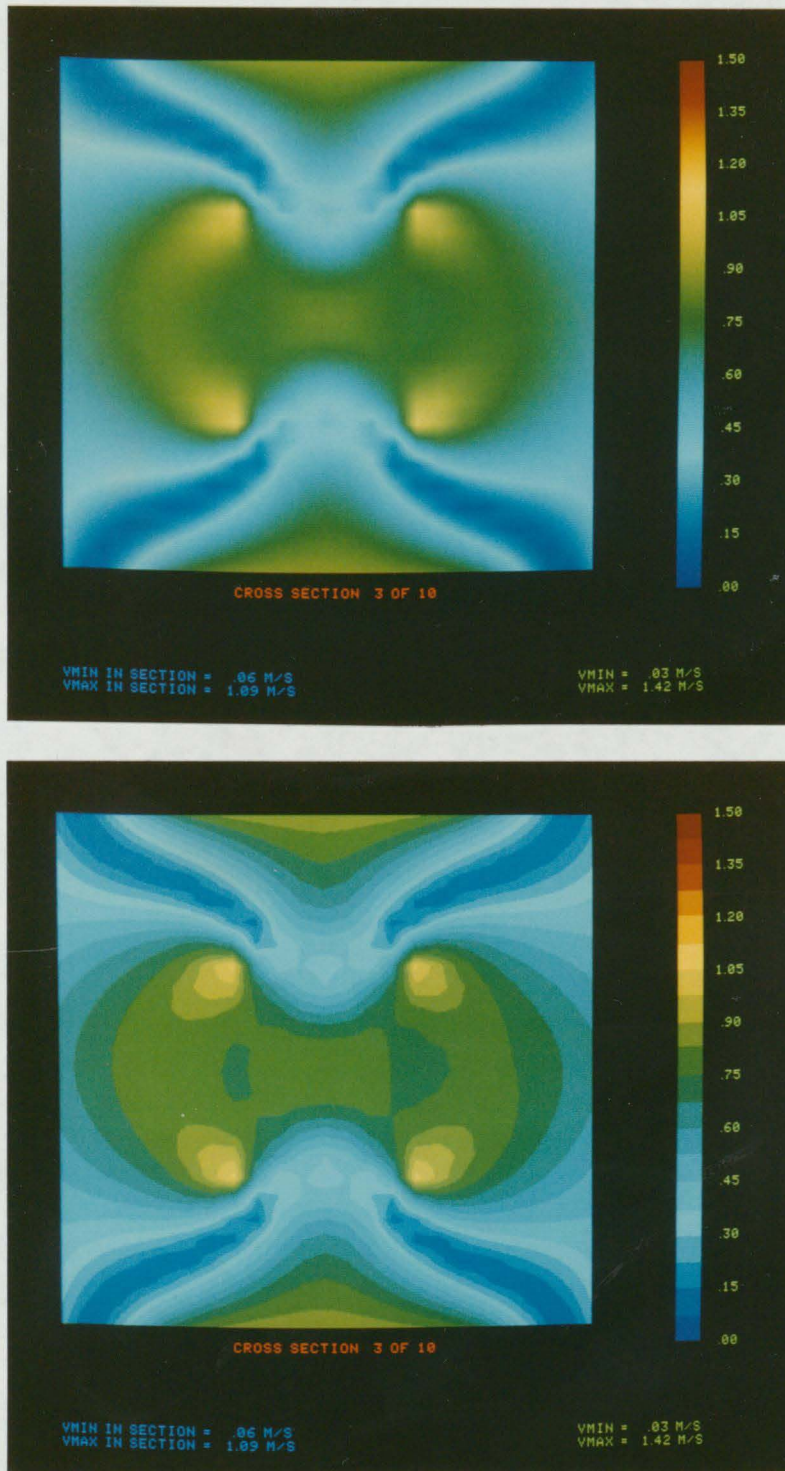


Figure 30. Full-screen display of a velocity map from figure 29 for a section near the bottom of the visible volume.

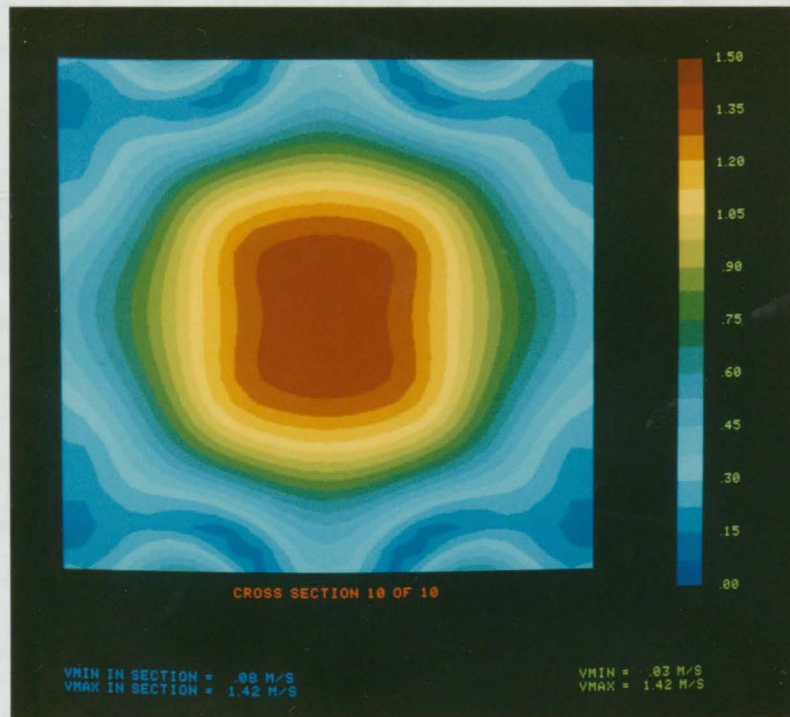
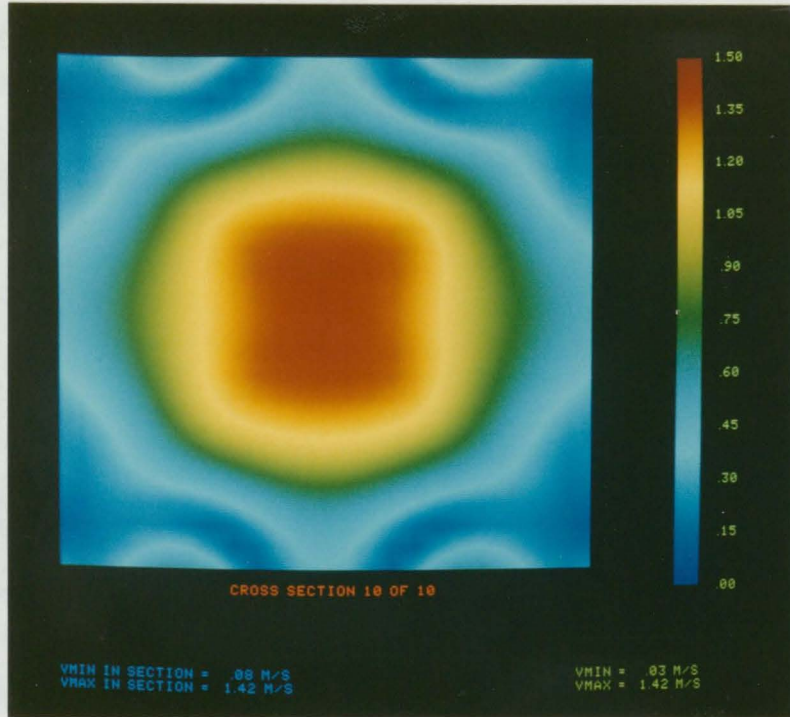


Figure 31. Full-screen display of a velocity map from figure 29 for the section at the top of the visible volume.

### 5.3 Evaluation of the method

From the tests that have been performed, both of each stage of the procedure using fictitious data and of the co-ordinated package using real flow data, the potential of this method for useful application in analyzing tracer-seeded flows appears substantial. The optical equipment required to obtain the perpendicular views is simple and poses relatively few alignment problems. The photogrammetric analysis of orthogonal scenes, with appropriate parallax correction, has good capacity to resolve tracer images and recognize correct matches. Trajectory tracing in three dimensions has proved to perform quite accurately, especially in cases where closely spaced trajectories could cause problems in methods based on two-dimensional tracking.

The individual components of the analysis protocol have been developed with sufficient built-in flexibility and mutual independence to allow a variety of data formats to be accepted. Experimental data can therefore be introduced at various stages in the process, be it at the image analysis stage (if film or video records are available), at the matching stage (for previously digitized tracer positions in orthogonal views) or at the tracking stage (if three-dimensional co-ordinates are already available). This suggests possible applications of the procedure to fields other than flow visualization, wherever there is need to analyze complex three-dimensional motions of various well-defined objects. In the area of ballistics, for instance, uses could be found for this type of automated analysis. Also, kinesiology studies that

utilize bright markers applied to different parts of a moving subject's body can benefit from a similar method.

The analysis procedure for fluid motion developed so far makes it possible to go from cine recordings of tracer seeded flows to time-resolved pathlines or eulerian velocity maps of the entire field in a virtually automatic fashion. As such, it constitutes a basic tool for studies of velocity profiles, pressure distribution, vortex formation in mixing processes, or flow stagnation in haemodynamics, to mention a few. Much improvement can be brought to the method by the use of a better visual interface, such as some of the video devices mentioned earlier in this thesis. The rapidly advancing field of video technology, both analog and digital, should soon make these devices more readily available and affordable. The computerized procedure itself can be optimized for a particular application so that the interactive features currently available may be bypassed. These features were essential in the development and testing of the method and give more flexibility to the analysis process, but require specialized apparatus, like an image processor, that may not be easily obtained. Again, evolving technology will make such equipment more commonplace in the next few years.

Bringing the capabilities of machine vision to the field of flow visualization is a challenging and promising endeavor. Along with particle tracking, other techniques such as dye diffusion are suitable for computerized analysis of the visual records, which eliminates the difficulties and inconsistencies of human interpretation. At the oppo-

site end of the process, the task of effectively displaying multi-dimensional results such as vector velocity fields so that the most information is conveyed with the least visual cluttering is a stimulating task in itself. The science of three-dimensional imaging, still evolving and tapping new resources, offers an open field for more research and application.

## BIBLIOGRAPHY

- Caffyn, J.E., Underwood, R.M. 1952. An Improved Method for the Measurement of the Velocity Profiles in Liquids. *Nature*, 169, 239-240.
- Chang, T.P., Tatterson, G.B. 1983. An Automated Analysis Method for Complex Three Dimensional Mean Flow Fields. Third International Symposium on Flow Visualization preprints, 266-273.
- Charwat, A.F. 1977. Motion of near-neutrally buoyant tracers in vortical flows. *The Physics of Fluids*, 20, 1401-1403.
- Dewey, J.M. 1971. The properties of a blast wave obtained from an analysis of the particle trajectories. *Proc. R. Soc. Lond. A*. 324, 275-299.
- Dutta, K., Jaffey, S.M. 1983. Time Smear Corrected Multiplex Holographic Display of Computerized Tomography Data. *SPIE Proceedings v. 402*, 88-94.
- Gonzalez, R.C., Wintz, P. 1977. Digital Image Processing. Addison-Wesley Publishing Co., Inc., Reading, Ma.
- Hall, E.L. 1979. Computer Image Processing and Recognition. Academic Press, Inc., New York.
- Hesselink, L., Pender, J., Jaffey, S., Dutta, K. 1983. Quantitative three-dimensional flow visualization. Third International Symposium on Flow Visualization preprints, 375-379.
- Hyzer, W.G. 1984. Simultaneous Orthogonal-View High-Speed Photography. *Imaging Technology in Research and Development*, July, 6-11.
- Peskin, C.S. 1972. Flow Patterns Around Heart Valves. Ph.D. Dissertation, Albert Einstein College of Medicine, Yeshiva University.
- Praturi, A.K., Brodkey, R.S. 1978. A stereoscopic visual study of coherent structures in turbulent shear flow. *J. Fluid Mech.*, 89, 251-272.
- Racca, R.G., Dewey, J.M. 1984. Automatic particle tracking in a three-dimensional flow field. *Proceedings of the 16th International Congress on High Speed Photography and Photonics*, (in print).
- Roberson, E.C. 1955. Report of the National Gas Turbine Establishment No. R.181.

- Sheu, Y.-H.E., Chang, T.P.K., Tatterson, G.B., Dickey, D.S. 1982. A three-dimensional measurement technique for turbulent flows. *Chem. Eng. Commun.*, 17, 67-83.
- Tatterson, G.B., Yuan, H.-H.S., Brodkey, R.S. 1980. Stereoscopic visualization of the flows for pitched blade turbines. *Chem. Eng. Sci.*, 35, 1369-1375.
- Taylor, J. 1976. CONMAP: A Computer Program for Contouring Oceanographic Data. Technical Note No. 12, Marine Environmental Data Service, Environment Canada, Fisheries and Marine Service.
- Taylor, J., Richards, P., Halstead, R. 1971. Computer Routines for Surface Generation and Display. Manuscript Report Series No. 16, Marine Sciences Branch, Dept. of Energy, Mines and Resources.
- Wieting, D.W. 1969. Dynamic Flow Characteristics of Heart Valves. Ph.D. dissertation, The University of Texas at Austin.
- Winter, E.F. 1958. Flow Visualization Techniques Applied to Combustion Problems. *Jl R. Aeronaut. Soc.*, 62, 268-276.

## APPENDIX A

Derivation of the 'rubber sheet' transformation

Consider a quadrilateral defined by points A, B, C, D at  $(x_a, y_a)$ ,  $(x_b, y_b)$ ,  $(x_c, y_c)$ ,  $(x_d, y_d)$  as shown in figure 32. The vertices are moved to points A', B', C', D' at  $(x'_a, y'_a)$ ,  $(x'_b, y'_b)$ ,  $(x'_c, y'_c)$  and  $(x'_d, y'_d)$ . For any internal point O at  $(x_o, y_o)$  we want to find the co-ordinates  $(x'_o, y'_o)$  of the corresponding point O' in the transformed surface.

Segments HK and LM are constructed through  $(x_o, y_o)$  so that they divide opposite sides in the same ratios, namely,

$$\frac{|DL|}{|DC|} = \frac{|AM|}{|AB|} \quad , \text{ and} \quad (\text{A.1})$$

$$\frac{|HD|}{|AD|} = \frac{|KC|}{|BC|} \quad . \quad (\text{A.2})$$

The segments HK and LM divide each other at O in the same ratios as they divide the corresponding sides. Hence we have the additional equations

$$\frac{|HO|}{|HK|} = \frac{|DL|}{|DC|} \quad , \text{ and} \quad (\text{A.3})$$

$$\frac{|LO|}{|LM|} = \frac{|HD|}{|AD|} \quad . \quad (\text{A.4})$$

Since all the ratios are between lengths of collinear segments, expressions (A.1) through (A.4) can be decomposed into separate equations in terms of distance components in the x and y directions. Four of these

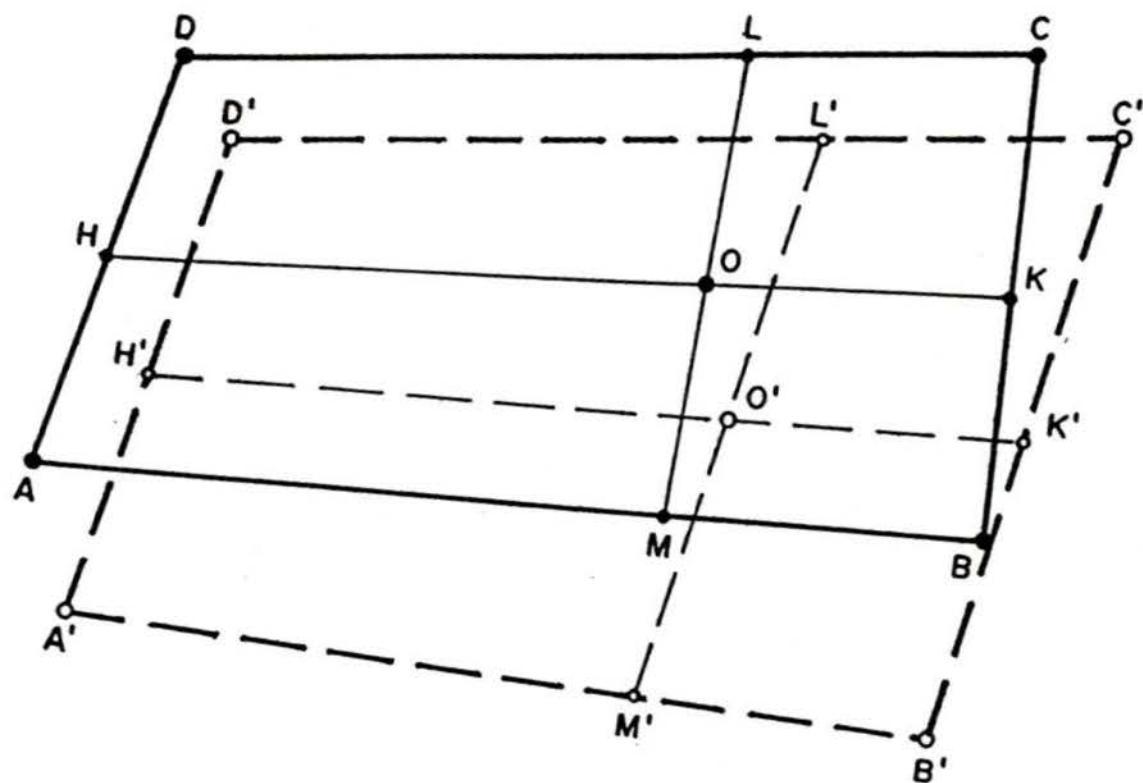


Figure 32. Geometrical layout for the 'rubber sheet' transformation equations.

equations form a system in the unknowns  $x_1, x_m, y_h, y_k$ :

$$\frac{x_1 - x_d}{x_c - x_d} = \frac{x_m - x_a}{x_b - x_a} \quad , \quad (\text{A.5})$$

$$\frac{y_d - y_h}{y_d - y_a} = \frac{y_c - y_k}{y_c - y_b} \quad , \quad (\text{A.6})$$

$$\frac{y_o - y_h}{y_k - y_h} = \frac{x_1 - x_d}{x_c - x_d} \quad , \quad \text{and} \quad (\text{A.7})$$

$$\frac{x_o - x_1}{x_m - x_1} = \frac{y_d - y_h}{y_d - y_a} \quad . \quad (\text{A.8})$$

The equations and unknowns in the above system were selected so that known denominators cannot be zero even if the original quadrilateral has some horizontal or vertical sides, provided corners are named as in figure 32. Eliminating all unknowns except  $x_1$ , we obtain a quadratic equation of the form

$$c_2 x_1^2 + c_1 x_1 + c_0 = 0 \quad , \quad (\text{A.9})$$

where

$$c_2 = (y_b - y_a) + \frac{x_a - x_b}{x_c - x_d} (y_c - y_d) \quad ,$$

$$c_1 = x_o(y_a - y_b + y_c - y_d) - y_o(x_a - x_b + x_c - x_d) + x_c y_a - x_d y_b + \frac{(x_b x_d - x_a x_c)(y_c - y_d) + (x_c y_d - x_d y_c)(x_a - x_b)}{x_c - x_d} \quad ,$$

$$c_0 = x_o[x_c(y_d - y_a) + x_d(y_b - y_c)] + y_o(x_c x_a - x_d x_b) + \frac{(x_c x_a - x_d x_b)(x_d y_c - x_c y_d)}{x_c - x_d} \quad .$$

For the case in which  $c_2$  is nonzero the above has two solutions, which may be coincident. If they are distinct, only the one containing the

negative square root of the discriminant falls between  $x_c$  and  $x_d$ , thus giving the desired geometrical construction. The other solution is not geometrically acceptable since it leads to a segment LM that lies entirely outside the quadrilateral ABCD and hence cannot contain the point O. Therefore,

$$x_1 = \begin{cases} \frac{-c_1 - \sqrt{c_1^2 - 4c_2c_0}}{2c_2} & \text{for } c_2 \neq 0 \\ -\frac{c_0}{c_1} & \text{for } c_2 = 0 \end{cases} \quad (\text{A.10})$$

Once  $x_1$  is computed, the other unknowns can be found using suitable combinations of equations (A.5) to (A.8). In fact, only  $y_h$  will be required along with  $x_1$  in the development that follows, so the other two may be ignored. The expression for  $y_h$  is

$$y_h = \frac{y_0(x_c - x_d) - (x_1 - x_d)(K_2 y_d + y_c)}{x_c - x_1 - K_2(x_1 - x_d)}, \quad (\text{A.11})$$

where

$$K_2 = \frac{y_b - y_c}{y_d - y_a}.$$

We can now make use of the fact that the segments HK and LM are transformed into segments H'K' and L'M' that divide the new opposite sides in the same ratios as HK and LM divide the original sides, namely,

$$\frac{|D'L'|}{|D'C'|} = \frac{|DL|}{|DC|}, \quad (\text{A.12})$$

$$\frac{|A'M'|}{|A'B'|} = \frac{|DL|}{|DC|}, \quad (\text{A.13})$$

$$\frac{|A'H'|}{|A'D'|} = \frac{|AH|}{|AD|} , \text{ and} \quad (\text{A.14})$$

$$\frac{|B'K'|}{|B'C'|} = \frac{|AH|}{|AD|} . \quad (\text{A.15})$$

Considering only x components in (A.12) and (A.13) and y components in (A.14) and (A.15) we obtain respectively

$$x'_j = \frac{x'_c - x'_d}{x_c - x_d} (x_1 - x_d) + x'_d , \quad (\text{A.16})$$

$$x'_m = \frac{x'_b - x'_a}{x_c - x_d} (x_1 - x_d) + x'_a , \quad (\text{A.17})$$

$$y'_h = \frac{y'_d - y'_a}{y_d - y_a} (y_h - y_a) + y'_a , \text{ and} \quad (\text{A.18})$$

$$y'_k = \frac{y'_c - y'_b}{y_d - y_a} (y_h - y_a) + y'_a . \quad (\text{A.19})$$

The segments H'K' and L'M' divide each other at O' in the same ratios as HK and LM divide each other at O, namely,

$$\frac{|H'O'|}{|H'K'|} = \frac{|HO|}{|HK|} , \text{ and} \quad (\text{A.20})$$

$$\frac{|L'O'|}{|L'M'|} = \frac{|LO|}{|LM|} . \quad (\text{A.21})$$

It may seem that by considering the x distance components in (A.20) and the y distance components in (A.21) we could get  $x'_0$  and  $y'_0$  in terms of quantities already computed. However, the resulting expressions would contain terms of the form  $(x_0 - x_1)/(x_m - x_1)$  and  $(y_0 - y_h)/(y_k - y_h)$ , and hence be undeterminate in the acceptable cases of  $x_1 = x_m = x_0$  or

$y_h = y_k = y_0$ . The solution is to consider the ratio of x components on the left hand side and the ratio of y components on the right hand side of (A.20), and the opposite for (A.21). The expressions for  $x'_0$  and  $y'_0$ , from (A.21) and (A.20) respectively, are then

$$x'_0 = \frac{x'_m - x'_1}{y'_m - y'_1} (y_0 - y_1) + x'_1 \quad , \text{ and} \quad (\text{A.22})$$

$$y'_0 = \frac{y'_k - y'_h}{x'_k - x'_h} (x_0 - x_h) + y'_h \quad . \quad (\text{A.23})$$

The yet unknown terms  $x_1$ ,  $x_m$ ,  $y_h$ ,  $y_k$  are easily computed from known quantities using conditions of collinearity:

$$x_h = \frac{x'_d - x'_a}{y'_d - y'_a} (y_h - y_a) + x_a \quad , \quad (\text{A.24})$$

$$x_k = \frac{x'_c - x'_b}{y'_d - y'_a} (y_h - y_a) + x_b \quad , \quad (\text{A.25})$$

$$y_1 = \frac{y'_c - y'_d}{x'_c - x'_d} (x_1 - x_d) + y_d \quad , \text{ and} \quad (\text{A.26})$$

$$y_m = \frac{y'_b - y'_a}{x'_c - x'_d} (x_1 - x_d) + y_a \quad . \quad (\text{A.27})$$

Using the values obtained from the above in (A.22) and (A.23) gives  $x'_0$  and  $y'_0$ . For all practical purposes, substitution of intermediate values in every step may be simply performed numerically.

The summary of the transformation is as follows: given  $(x_a, y_a)$  to  $(x_d, y_d)$ ,  $(x'_a, y'_a)$  to  $(x'_d, y'_d)$ , and  $(x_0, y_0)$ ,

- Compute  $x_1$  from (A.10),
- Compute  $y_h$  from (A.11),

- Compute  $x_1^i, x_m^i, y_h^i, y_k^i$  from (A.16) to (A.19),
- Compute  $x_h, x_k, y_1, y_m$  from (A.24) to (A.27), and
- Compute  $x_0^i$  and  $y_0^i$  from (A.22) and (A.23).

## APPENDIX B

Derivation of the parallax correction equations

Consider two perpendicular picture planes, containing the  $z$  axis and respectively the  $x$  axis and the  $y$  axis, as shown in figure 33. The viewpoints  $V'$ ,  $V''$  are located at distance  $D$  from their corresponding image plane, along the lines  $(x = d_a, z = z_a)$  and  $(y = d_a, z = z_a)$ . A point located at  $(x, y, z)$  will be projected at position  $(x', z')$  on the plane  $y = 0$  and at position  $(y'', z'')$  on the plane  $x = 0$ . From elementary geometry we obtain the relations

$$x' = d_a + \frac{D(x - d_a)}{D + y} \quad , \quad (\text{B.1})$$

$$y'' = d_a + \frac{D(y - d_a)}{D + x} \quad , \quad (\text{B.2})$$

$$z' = z_a + \frac{D(z - z_a)}{D + y} \quad , \quad \text{and} \quad (\text{B.3})$$

$$z'' = z_a + \frac{D(z - z_a)}{D + x} \quad . \quad (\text{B.4})$$

Rearrangement of terms yields the inverse relations

$$x = x' + \frac{y}{D} (x' - d_a) \quad , \quad (\text{B.5})$$

$$y = y'' + \frac{x}{D} (y'' - d_a) \quad , \quad (\text{B.6})$$

$$z = z' + \frac{y}{D} (z' - z_a) \quad , \quad \text{and} \quad (\text{B.7a})$$

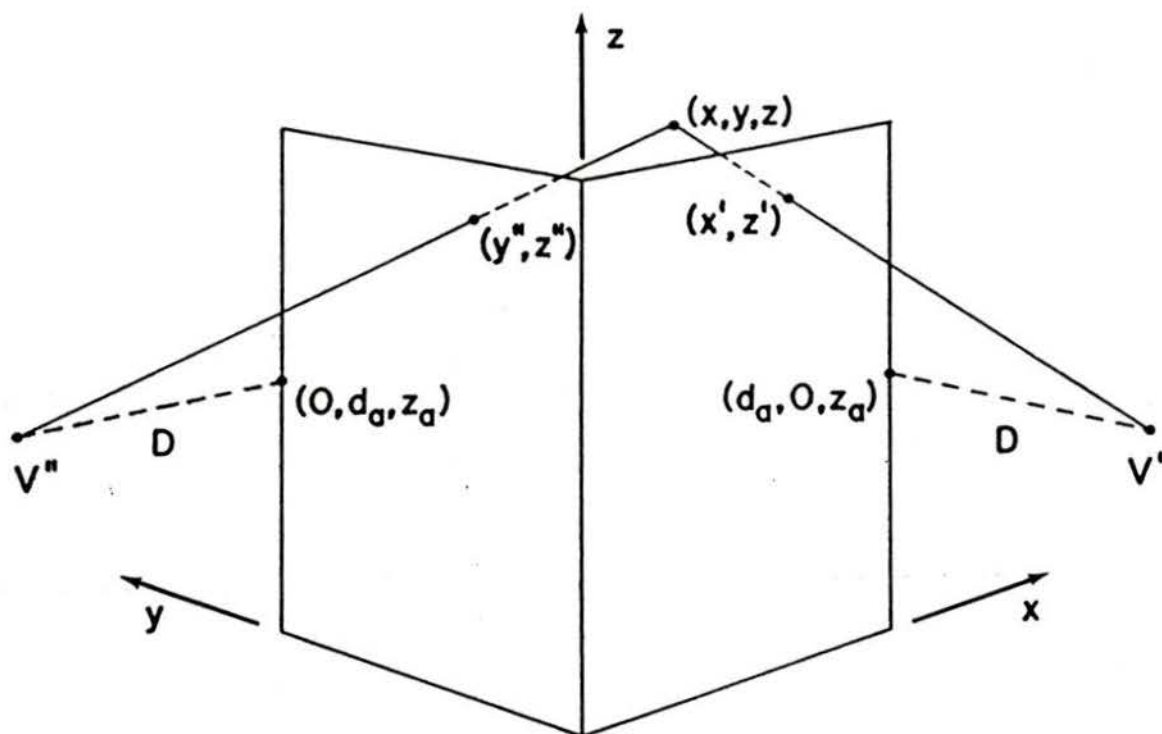


Figure 33. Geometrical layout for the parallax correction equations.

$$z = z'' + \frac{x}{D} (z'' - z_a) \quad . \quad (\text{B.7b})$$

Equation (B.6) can be used to substitute for  $y$  in (B.5). The resulting expression for  $x$  is

$$x = \frac{D^2 x' + D y'' (x' - d_a)}{D^2 - (y'' - d_a)(x' - d_a)} \quad . \quad (\text{B.8})$$

In a similar fashion we obtain an expression for  $y$ :

$$y = \frac{D^2 y'' + D x' (y'' - d_a)}{D^2 - (y'' - d_a)(x' - d_a)} \quad . \quad (\text{B.9})$$

Substitution in (B.7a) and (B.7b) gives independent expressions for  $z$ :

$$z = z' + \frac{D y'' + x' (y'' - d_a)}{D^2 - (y'' - d_a)(x' - d_a)} (z' - z_a) \quad , \text{ and} \quad (\text{B.10a})$$

$$z = z'' + \frac{D x' + y'' (x' - d_a)}{D^2 - (y'' - d_a)(x' - d_a)} (z'' - z_a) \quad . \quad (\text{B.10b})$$

In practice, after evaluating (B.8) it is more convenient to use equations (B.6), (B.7a) and (B.7b) and substitute numerically intermediate results than to use the fully substituted expressions.

VITA

Surname: RACCA Given names: ROBERTO GIACOMO

Place of Birth: Cuneo, Italy Date of Birth: January 9, 1960

Educational Institutions Attended, with Dates of Entering and Leaving:

CAMOSUN COLLEGE, VICTORIA, B.C. 1977 to 1978

UNIVERSITY OF VICTORIA, VICTORIA, B.C. 1978 to 1985

Degrees, Diplomas, Etc., Awarded, with Dates and Names of Institutions:

B.Sc. (Honours) 1982 University of Victoria

Honors and Awards:

Seaspan International Ltd. Scholarship, 1978/79

The Edward J. Savannah Memorial Scholarship, 1978/79

Publications:

Racca, R.G., Dewey, J.M. 1984. Automatic particle tracking in a  
three-dimensional flow field. Proceedings of the 16th International  
Congress on High Speed Photography and Photonics, (in print).

Walker, D.K., Scotten, L.N., Hewgill, D.E., Racca, R.G., Brownlee, R.T.  
1983. Development and in vitro assessment of a new two-leaflet  
replacement heart valve designed using computer-generated bubble  
surfaces. Med. & Biol. Eng. & Comput. 21, 31-38.

Brownlee, R.T., Scotten, L.N., Walker, D.K., Hewgill, D.E., Racca, R.G.  
1983. Two-leaflet mitral bioprosthesis - design and in vitro  
performance. Canadian Cardiovascular Society meeting, Toronto,  
Canada.

Walker, D.K., Scotten, L.N., Racca, R.G., Brownlee, R.T. 1983.  
Acquisition and analysis of data obtained from the in vitro testing  
of replacement heart valves. AAMI 18th annual meeting, Dallas, USA.

Scotten, L.N., Racca, R.G., Nugent, A.H., Walker, D.K., Brownlee, R.T.  
1981. New tilting disc cardiac valve prostheses - In vitro  
comparison of their hydrodynamic performance in the mitral position.  
J. Thor. Cardiovasc. Surg. 82, 136-146.


PARTIAL COPYRIGHT LICENSE

I hereby grant the right to lend my thesis (the title of which is shown below) to users of the University of Victoria Library, and to make single copies only for such users or in response to a request from the Library of any other university, or similar institution, on its behalf or for one of its users. I further agree that permission for extensive copying of this thesis for scholarly purposes may be granted by me or a member of the University designated by me. It is understood that copying or publication of this thesis for financial gain shall not be allowed without my written permission.

Title of Thesis

AUTOMATIC PARTICLE TRACKING IN A THREE-DIMENSIONAL FLOW FIELD

Author

  
ROBERTO G. RACCA

June 27, 1985